



**HAL**  
open science

## Seafloor depressions on the Nigerian margin: Seabed morphology and sub-seabed hydrate distribution

F. Taleb, M. Lemaire, S. Garziglia, T. Marsset, N. Sultan

### ► To cite this version:

F. Taleb, M. Lemaire, S. Garziglia, T. Marsset, N. Sultan. Seafloor depressions on the Nigerian margin: Seabed morphology and sub-seabed hydrate distribution. *Marine and Petroleum Geology*, 2020, 114, pp.104175 -. 10.1016/j.marpetgeo.2019.104175 . hal-03488690

**HAL Id: hal-03488690**

**<https://hal.science/hal-03488690>**

Submitted on 21 Jul 2022

**HAL** is a multi-disciplinary open access archive for the deposit and dissemination of scientific research documents, whether they are published or not. The documents may come from teaching and research institutions in France or abroad, or from public or private research centers.

L'archive ouverte pluridisciplinaire **HAL**, est destinée au dépôt et à la diffusion de documents scientifiques de niveau recherche, publiés ou non, émanant des établissements d'enseignement et de recherche français ou étrangers, des laboratoires publics ou privés.



Distributed under a Creative Commons Attribution - NonCommercial 4.0 International License

1 **Seafloor depressions on the Nigerian margin: seabed morphology and sub-**  
2 **seabed hydrate distribution**

3 **F. Taleb<sup>1</sup>, M. Lemaire<sup>2,3</sup>, S. Garziglia<sup>1</sup>, T. Marsset<sup>1</sup> and N. Sultan<sup>1</sup>**

4

5 <sup>1</sup>*IFREMER, Département REM, Unité des Géosciences Marines, F-29280 Plouzané, France*

6 <sup>2</sup>Université de Lille, CNRS, UMR 8523 - PhLAM- Physique des Lasers Atomes et Molécules, F-59000  
7 Lille, France

8 <sup>3</sup>Université de Bordeaux, CNRS UMR 5255 ISM- Institut des Sciences Moléculaires, 33405 Talence,  
9 France.

10

11 Corresponding author: Farah Taleb (farah.taleb@ifremer.fr)

12

13 Highlights:

- 14 • Mineralogical analysis is essential if estimating GH content using in-situ data
- 15 • 3D scheme of the pockmark and GH occurrence zone created from seismic data
- 16 • The geomorphology of the study area is influenced by GH content and distribution

17 **Abstract**

18 Gas hydrate quantification using acoustic data requires proper knowledge of the mineralogy of their  
19 host sediment. In this paper, a petrophysical model allowing GH quantification at sites where  
20 mineralogy profiles are absent is proposed. This approach is applied to a high gas flux pockmark  
21 system in the Gulf of Guinea where in-situ acoustic and geotechnical measurements together with  
22 core measurements could have been correlated and tied to seismic data. Projections of the in-situ  
23 measurements on seismic profiles have shown that the study area not only accommodates zones of  
24 shallow and dense GH; but also zones where solid hydrate and free gas coexist as well as pockets of  
25 free gas. Further analysis of several seismic profiles has allowed illustrating the detailed GH  
26 occurrence zone within the study area, estimate its volume and its occupancy ratio of the pockmark.  
27 Correlations between GH content and 3D bathymetry sections have allowed to draw a link between  
28 different GH contents and the morphology of the pockmark, which also shares similarities with the  
29 morphology of the GH occurrence zone it accommodates.

30

31 *Keywords: Gas hydrates quantification, Pockmarks, in-situ measurements, seismic profiles, GH*  
32 *distribution, petrophysical model, clayey sediments.*

## 33 1. Introduction

34 Gas hydrate (GH) are ice-like solid mixtures of gas molecules, mainly methane, trapped within a  
35 crystalline structure of water molecules (*Sloan, 1998*). These geo-compounds are stable under  
36 high pressure and low temperature within a depth range known as the GH stability zone. Their  
37 presence also requires continuous supply of gas with a concentration exceeding the solubility  
38 limit in water and sufficient amount of water (*Sultan et al., 2010*). They have been mainly  
39 inferred and recovered along continental margins and polar permafrost layers (*Kvenvolden,*  
40 *1993*). GH represent the largest stock of natural gas in the world (*Shankar et al., 2013*), but also a  
41 geotechnical hazard threatening offshore operations as well as potential agent of climate  
42 change. This made them a target for many scientific and industrial interests.

43 Understanding the effect of GH on their host sediment behaviour requires knowledge of their  
44 physical characteristics, properties, concentration and morphology. *Holland et al. (2008)* showed  
45 that the morphology of GH is a means of describing the relation between GH and their bearing  
46 sediment as well as defining the physical properties of the sediment-hydrate matrix.

47 GH are known to be metastable; thus, their identification and characterisation through actual  
48 recovery of core samples have been proved challenging (*Dai et al., 2012*). Therefore, as  
49 previously shown by *Sultan et al. (2014; 2010)* and *Taleb et al. (2018)*, in this work the detection  
50 of GH has been inferred via in-situ measurements.

51 These measurements are eventually interpreted using an effective medium theory (EMT). The  
52 latter, establishes a relation between the compressional wave velocity anomalies, the mineralogy  
53 of the host sediment and the hydrate morphology and fraction (*Helgerud et al., 1999*).

54 Many research studies used this method in order to quantify GH in marine sediments. For  
55 instance, *Carcione and Gei (2004)*, used the EMT in order to estimate concentrations of GH in the  
56 Mallik 2L-38 research well, Canada. Results derived from P and S wave velocities were found  
57 comparable to those obtained from Archie's method. Additionally, *Chand et al. (2004)* have  
58 showed that for clayey sediments at ODP sites 995 and 997, the EMT results are highly

59 comparable with those derived from electrical resistivity. Moreover, it was observed that for a  
60 clay-hydrate system, it is more suitable to assume that hydrates affect the rock framework rather  
61 than the pore fluid. [Guerin et al. \(1999\)](#) investigated GH occurrence in the Blake Ridge (ODP  
62 Program Leg 164), where it was observed that hydrates increase the bulk modulus of the host  
63 sediment. The rest of the results showed that GH estimates derived from assuming that hydrates  
64 are acting as a cementing agent are very comparable to those derived from resistivity logs. [Kim  
65 et al. \(2013\)](#) predicted GH contents using the EMT in the Ulleung Basin, which were later  
66 compared to results from electrical resistivity and from an empirical Archie-analysis. Results have  
67 shown that using EMT with a detailed mineralogy is a reliable method when estimating GH  
68 contents. [Wang et al. \(2011\)](#) used the EMT and compared it to other quantification methods such  
69 as chlorinity analysis and electrical resistivity within the clayey sediments of the Shenhu area,  
70 South China Sea. Compared with other methods, results from the EMT were found rather  
71 satisfactory.

72 The presence of GH in the marine environment dramatically alters the physical properties of the  
73 host sediment by replacing the pore water /or gas with a solid compound. The compressional  
74 wave velocity of GH-bearing sediments is much higher than that of sediments without hydrate.  
75 On the contrary, free-gas bearing sediments tend to show negative compressional velocity  
76 anomalies.

77 Those different approaches are often based on a well-known mineralogy of the host sediment  
78 column (by coring or drilling) and on the difference between a reference sonic velocity profile  
79 with respect to the one altered by the presence of free gas and GH. However, the use of in-situ  
80 acoustic measurements to quantify GH as proposed by [Sultan et al. \(2010\)](#) is restricted by the  
81 requirement to characterise the in-situ mineralogy of the host sediment.

82 Previously, [Taleb et al. \(2018\)](#) have discussed the effect of GH content and morphology on the  
83 hydro mechanical properties of their host clayey sediments. In order to carry out this work, GH  
84 quantification at certain measuring sites was conducted using the EMT. The aim of the present

85 paper is to expand on this previous work, especially by integrating the results of in-situ  
86 measurements with seismic data. This is achieved through a detailed review of the different  
87 steps followed in order to use the EMT, with special emphasis on the establishment of a  
88 petrophysical model and the derivation of mineralogical profiles from in-situ acoustic attenuation  
89 data. This was carried out by performing correlations between different laboratory and in-situ  
90 data before comparing the similarities and the differences between reference sites without GH  
91 and GH-bearing sites. This proved effective in detecting and quantifying GH based on in-situ  
92 acoustic measurements even for sediments where accurate mineralogical characterisation is not  
93 available.

94 Numerous oceanographic campaigns, aiming to study GH distribution, have been carried out  
95 along the Gulf of Guinea, which is known to accommodate dense accumulations of shallow GH  
96 (*Cunningham and Lindholm, 2000; Sultan et al., 2010; Wei et al., 2015*). The study area is also  
97 characterised by the presence of different seabed deformations known as pockmarks. However,  
98 little has been discussed concerning the distribution of GH below the seabed and its impact on  
99 the shapes and sizes of these pockmarks. As a step towards identifying links between GH and  
100 free gas and the geometrical features of different pockmarks, the second aim of this paper is to  
101 correlate seismic data profiles and seabed morphologies with GH content. Analysing the  
102 geophysical signatures of GH accumulations and extrapolating all the available in-situ data using  
103 seismic profiles would indeed be helpful in the process of (1) characterising the sub-seafloor  
104 distribution of GH and (2) determining the relationship between hydrate distribution and  
105 seafloor depressions.

## 106 **2. Study area**

107 The study area is located in the Gulf of Guinea, in the southern part of Nigeria, off the Niger  
108 Delta. Numerous studies have shown that this area is characterised by various seabed  
109 features such as pockmarks which were directly linked to the formation and dissolution of GH

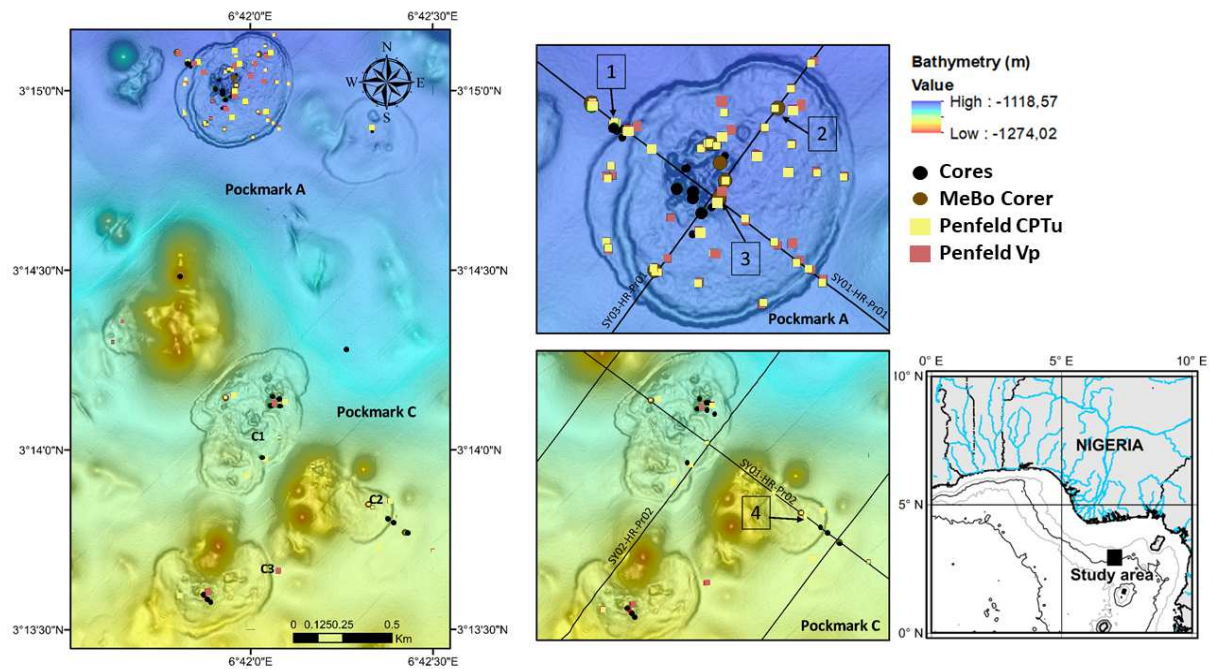
110 *(Sultan et al., 2014)*. The GH stability zone in the study area was found to expand from 90  
111 mbsf to 120 mbsf as reported by *Sultan et al. (2010)*.

112 This paper focuses on two specific pockmarks that are referred to as A and C. Pockmark A is  
113 situated in the northern part of the study area at depths lying between 1100 and 1200m  
114 (Figure 1). It is 600 meters in diameter with a 6 meters deep peripheral depression.  
115 Pockmark C is composed of a cluster of three sub-pockmarks revealing irregular seabed  
116 morphologies: C1, C2 and C3 (Figure 1) located at water depths ranging from 1170 m and  
117 1210 m. All four pockmarks are characterised by numerous moats and bumps on their  
118 surface. While the area is classified as a high gas flux system fed by deeply sourced gas  
119 through faults and fractures *(Sultan et al., 2016)*, GH have only been identified within  
120 pockmarks.

121 *Wei et al. (2015)* have defined GH occurrence zones (GHOZ) based on pore water chloride  
122 analyses and infrared thermal imaging. *Sultan et al. (2010)* have shown that the study area  
123 accommodates shallow GH formation and identified zones where solid GH and free gas  
124 coexist.

### 125 **3. Tools and methods**

126 Several cruises have been conducted in order to characterise the presence of GH in the study  
127 area. The Guineco-MeBo (2011) and ERIG3D (2008) oceanographic campaigns took place on the  
128 French R/V '*Pourquoi pas?*' and the NERIS2 (2004) on the R/V '*Atalante*'. All campaigns aimed to  
129 determine the distribution of GH in the study area in order to understand the link between GH  
130 and the mechanisms/formation and evolution of pockmarks as well as study the stability of  
131 sedimentary bodies.



132

133 *Figure 1. Bathymetry of the study area showing seismic profiles through pockmarks and the investigated sites: 1:*  
 134 *GMPFV07S05, GMMB01 and GMCS05, 2: GMPFV03S03 and GMMB12, 3: GMPFV07S05, GMMB06 and ERCS02 and 4:*  
 135 *GMPFV10S04 and GMMB05*

Penfeld Vp site	Depth (m)	Length (m)	Nearby Calypso or MeBo cores	Site	Location
GMPFV07S01	1140	30	GMMB01 GMCS05	1	NE - Outside of pockmark A
GMPFV03S03	1142	101.3	GMMB12	2	NW pockmark A
GMPFV07S05	1146	8.5	GMMB06 ERCS02	3	Centre of pockmark A
GMPFV10S04	1195	26	GMMB05	4	Eastern part of pockmark C2

136 *Table 1. Investigated sites within the study area: site 1 cluster characterises reference sediment without GH nor free gas*

137 *while clusters 2, 3 and 4 represent sediment where the presence of GH was suspected or proved.*

138        **3.1 In-situ measurements and coring**

139        3.1.1 Piezocone (Penfeld)

140        The Penfeld seabed rig developed by Ifremer was used to carry out the in-situ measurements.  
141        Continuous measurements were ensured by the penetration of a rod down to 30m below seabed at  
142        a standard rate of 2cm/s with a thrust of 40 kN (*Sultan et al., 2010*). The rod can push two types of  
143        probes into the sediment to carry out piezocone or acoustic soundings.

144        Pressure compensated sensors in the piezocone include two different load cells to measure the  
145        tip resistance ( $q_c$ ) and the sleeve friction ( $f_s$ ) along with a differential pore pressure ( $\Delta u_2$ )  
146        sensor located immediately behind the cone ( $u_2$  position).

147        Acoustic measurements can alternatively be carried out using the ultrasonic fork also pushed into the  
148        sediment at the rate of 2cm/s. One branch of the fork contains a 1MHz compressional wave source  
149        while the second one, located 7cm apart, and contains the receiver. This eventually allows measuring  
150        the velocity of compressional waves ( $V_p$ ) up to 2200 m/s together with the attenuation ratio  
151        between the emitted and received signal. In addition, the load applied to push the fork in the  
152        sediment is continuously measured during acoustic sounding.

153        In this paper four Penfeld  $V_p$  were investigated as shown in Figure 1 and in Table 1: site 1:  
154        GMPFV07S01 (outside pockmark A), site 2: GMPFV03S03 (NW sector of pockmark A), site 3:  
155        GMPFV07S05 (centre of pockmark A) and site 4: GMPFV10S04 (eastern part of pockmark C).

156        3.1.2 Coring and drilling

157        Cores were recovered using the Calypso piston coring system from Ifremer and the seafloor drill rig  
158        MeBo from Marum (*Freudenthal and Wefer, 2007; Freudenthal and Wefer, 2015*).

159        In this paper four MeBo cores (site1: GMMB01, site2: GMMB05, site 3: GMMB06 and site 4:  
160        GMMB12) and two Calypso cores (site 1: GMCS05 and site 3: ERCS02) allowed the investigation of  
161        the study area (Figure 1 and Table 1). These sites were particularly chosen because they are the  
162        closest to the  $V_p$  sites presented above; and therefore, the most comparable ones.

## 163 **3.2 Laboratory testing**

### 164 3.2.1 Multi Sensor Core Logging (MSCL), Acoustic measurements, X-ray diffraction (XRD) and X- 165 ray fluorescence (XRF)

166 The P-wave velocity, Gamma density and magnetic susceptibility were measured on board using the  
167 MSCL (Geotech). Measurements were done every centimetre for cores without hydrate and every 2  
168 cm for cores containing hydrate. In this paper, the density profile from core GMCS05 (site 1 in Figure  
169 1) was taken as a reference. Additionally, an acoustic fork, similar to that used in-situ with the  
170 Penfeld was used in order to determine the acoustic properties of the sediment in the laboratory.

171 The mineralogical composition of core GMCS05 was determined using the X-ray diffraction (XRD)  
172 technique every 10cm. Besides, the geochemical composition of the sediment was determined on  
173 the archive halves of each core at a sampling interval of 2cm using an Avaatech X-ray fluorescence  
174 (XRF) core scanner. This test can be performed at 10KV and 30KV, which allows the detection of  
175 different chemical elements.

176 Correlating results from both methods (XRF and XRD) allowed determining the mineralogical  
177 fractions every 2 cm of core GMCS05 ([see chapter 4.1.1: Mineralogy derived from XRF and XRD tests](#))

178 The XRF logging results were also interpreted in combination with acoustic measurements to  
179 determine the clay, calcite and quartz content within the sediment ([see chapter 4.1.2: Mineralogy  
180 derived from in-situ acoustic measurements](#))

## 181 **3.3 Seismic Survey**

182 The SYSIF (SYstème Sismique Fond de mer) is a deep-towed seismic system designed by Ifremer for  
183 high (HR: 250 – 1000 Hz) to very high resolution (VHR: 650 – 2000 Hz) near-bottom marine seismic  
184 surveys (*Marsset et al., 2010*). The penetration depth below the seabed is inversely proportional to  
185 the resolution quality and depends on the type of the penetrated sediment. Its altitude above the  
186 seabed is set at 100 m to reduce the Fresnel area where the pressure field is very irregular, which  
187 improves the lateral resolution with respect to the surface (*Ker et al., 2012*).

188 In the study area, several perpendicular SYSIF profiles have been acquired through pockmark A and  
189 C, which were used to correlate the acoustic/geotechnical data and the geomorphology of the  
190 pockmarks. This allowed understanding the distribution of GH and free gas within the pockmarks.  
191 Additionally, sub-bottom profiles were acquired every 4 meters using an Autonomous Underwater  
192 Vehicle (AUV) in pockmark A with an average penetration depth of around 70 meters. The AUV  
193 system produces pulses of 2-16 kHz, which are continuously narrowed in order to get a constant  
194 resolution with increasing depth. These pulses are then correlated with the recorded seismic data  
195 allowing enhancing the vertical resolution. The system is efficiently designed to minimize the survey  
196 time and maintain the same measuring speed (*George and Cauquil, 2007*); thus, resulting in an  
197 evenly dispersed data. This eventually allowed creating a 3D seismic data cube of the pockmark  
198 bathymetry and the GH0Z occupying this pockmark.

### 199 **3.4 GH quantification**

#### 200 3.4.1 From pore-water chloride analysis

201 During GH formation, chloride ions are excluded from the clathrate cage (*Ussler and Paull, 2001*);  
202 thus, salinity increases in the surrounding pore water. Therefore, upon core recovery, the  
203 dissociation of GH releases fresh water, which induces as negative anomalies on the pore-water  
204 chloride profiles (*Wei et al., 2015*). Pore water was extracted using Rhizon samplers on 12 MeBo  
205 cores and then chloride concentrations were determined using ion chromatography while assuming  
206 the absence of sulfate (*Wei et al., 2015*).

207 *Malinverno et al. (2008)* presented a method to estimate GH content ( $S_h$ ) from chloride anomalies:

$$208 S_h = \frac{\beta(C_{cb}-C_{cm})}{C_{cm}+\beta(C_{cb}-C_{cm})} \quad (1)$$

209 Where  $\beta$  is a coefficient that accounting for density change and equals 1.257,  $C_{cb}$  is the pore water  
210 chlorinity before GH dissociation measured in near-surface sediments and  $C_{cm}$  is the core chlorinity  
211 measured after GH dissociation.

212 *Malinverno et al. (2008)* described the  $C_{cb}$  parameter as critical to determine. Indeed the rapid in-  
 213 situ formation of GH, which translates into positive chloride anomalies, can affect the baseline  
 214 salinity prior to core recovery. The estimation of the baseline chlorinity at each GH-bearing site was  
 215 not possible. The lack of such information poses limitations for this method. Therefore, in this work,  
 216 the baseline chlorinity was defined based on a reference site where no gas hydrates nor free gas  
 217 were detected as seen in *Wei et al. (2015)*.  $C_{cb}$  values were observed to oscillate around 550 mM.

#### 218 3.4.2 From in-situ Vp measurements and rock physics characterisation

219 In this work, the EMT developed by *Helgerud et al. (1999)* has been used to estimate GH content in  
 220 the sediment by relating the stiffness of the dry frame to porosity, mineralogy and effective stress.  
 221 The model allows estimating a lower ( $S_{hmin}$ ) and upper bound ( $S_{hmax}$ ) of hydrate content, by  
 222 alternatively assuming that a) hydrate alters only the pore fluid elastic properties ( $S_{hmax}$ ); b) hydrate  
 223 contributes stiffness to the sediment by becoming part of the load-bearing framework ( $S_{hmin}$ )  
 224 (*Helgerud et al., 1999; Taleb et al., 2018*).

225 Input parameters such as the porosity and the mineralogy profile were determined from sediment  
 226 core GMCS05 (site 1 in Figure 1). [Table 2](#) shows the elastic properties and density used in this paper  
 227 (*Helgerud et al., 1999*)

Constituent m	$K(GPa)$	$G(GPa)$	$\rho(g/cm^3)$
Clay	20.9	6.85	2.58
Calcite	76.8	32	2.71
Quartz	36.6	45	2.65
GH	7.9	3.3	0.90
Water	2.4-2.6	0	1.032
Methane Gas	0.10-0.12	0	0.23

228 *Table 2. Elastic and density properties of selected sediment components (after Helgerud et al. 1999). K is the bulk modulus,*  
 229 *G the shear modulus and  $\rho$  the density.*

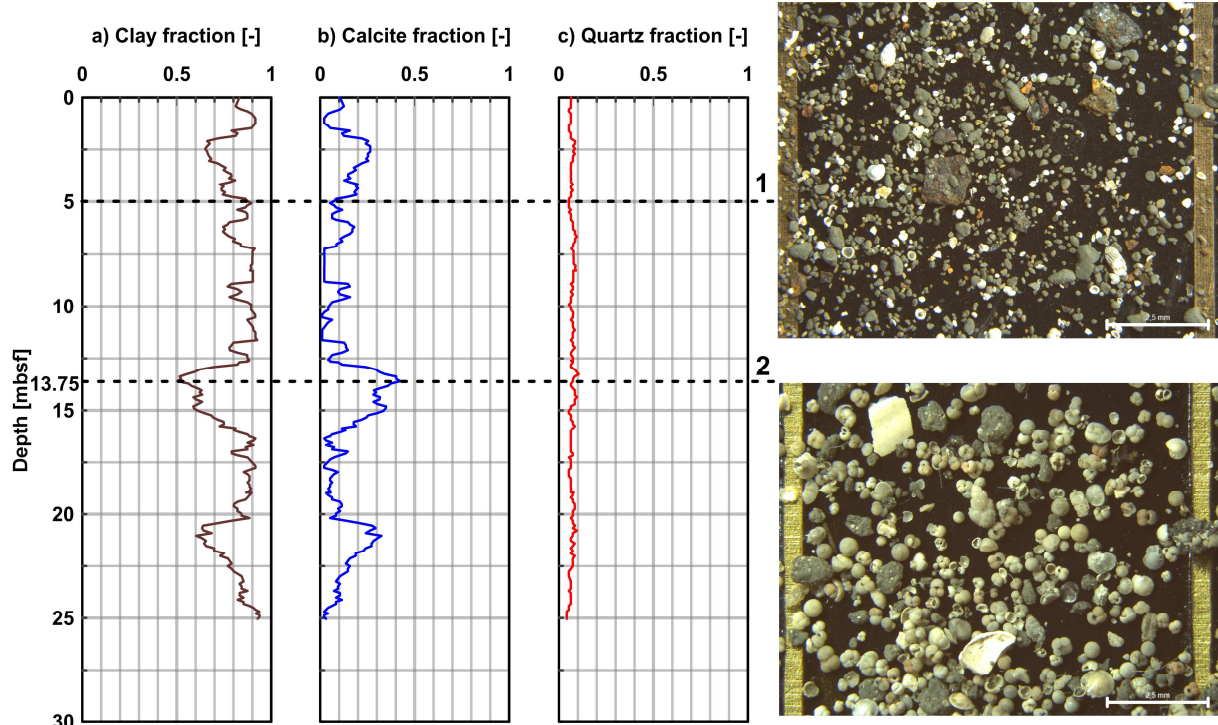
230 **4. Results**

231 **4.1 Mineralogical Analysis**

232 In order to apply the EMT and quantify the concentration of hydrates in sediments, the  
233 mineralogy profile characterising the sediment in question must be defined.

234 The mineralogical composition of the reference sediment from site GMCS05 is presented in  
235 [Figure 2](#), where it can be observed that the profile is dominated by clay and calcite with a low  
236 quartz fraction. While the clay fraction varies between 0.5 and 0.93, the calcite fraction varies  
237 between 0.01 and 0.42 and the quartz fraction is observed to have a quasi-constant value of  
238 around 0.06 with depth. Microscopic observations of the particle fraction larger than 63  $\mu\text{m}$   
239 reveal that fluctuations in calcite content are related to the foraminifera content and not to the  
240 presence of authigenic carbonates (Figure 2).

241 These XRD results were compared to those acquired with the XRF method in an attempt to  
242 obtain mineralogy profiles with a spacing of 2cm along cores.



243  
244 *Figure 2. Mineralogy profile for reference site GMCS05 (site 1 in [Figure 1](#)): a) clay fraction, b) calcite fraction and c) quartz*  
245 *fraction. Pictures to the right show the particule fractions larger than 63  $\mu\text{m}$  to be dominated by: 1) Rare benthic*

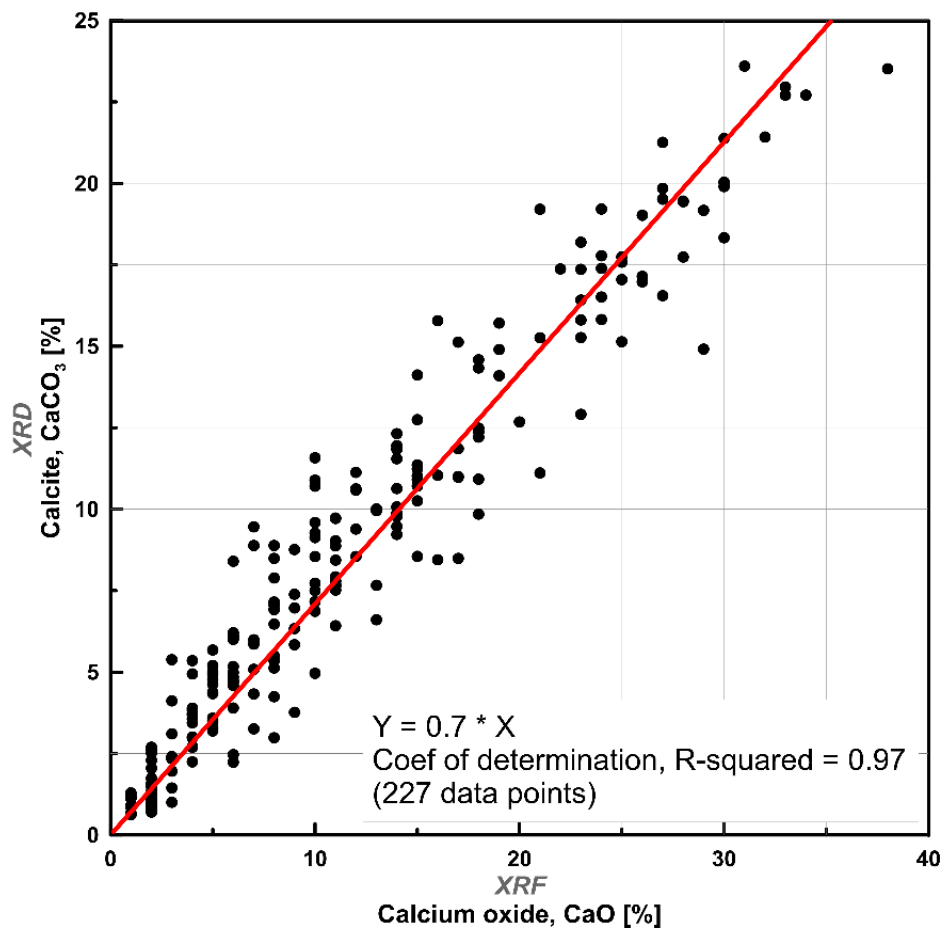
246 foraminifera *Uvigerina peregrina*, *Gyroidina* sp. and 2) Abundant planktonic foraminifera *Globigerinoides ruber*,  
247 *Globorotalia menardii*, *Neoglobloquadrina dutertrei*

#### 248 4.1.1 Mineralogy derived from XRF and XRD tests

249 Correlations between XRD and XRF for reference core GMCS05 (site 1 in Figure 1) showed that the  
250 concentration of calcite ( $\text{CaCO}_3$ ) can be linearly related to that of calcium oxide ( $\text{CaO}$ ) (Figure 3).  
251 Therefore, the following equation was proposed to determine the proportions of calcite based on the  
252 calcium oxide content in cases where the former is not available:

$$253 \text{CaCO}_3 (\%) = A \times \text{CaO} (\%) \quad (2)$$

254 Where A is the slope of the fitting line and is equal to 0.7 (red line in Figure 3)



255

256 Figure 3. Correlation of calcite fraction with calcium oxide fraction for core GMCS05

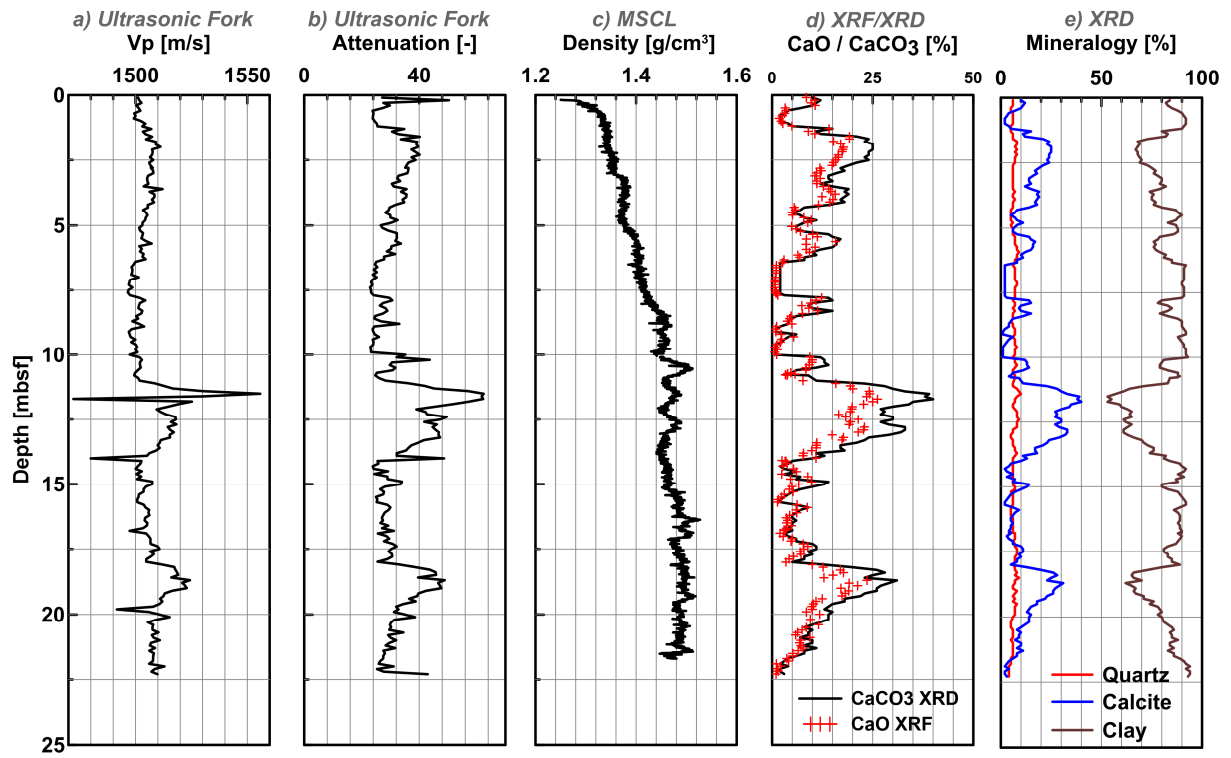
257 To further discuss the results at this stage, correlations between the mineralogical composition and  
258 acoustic data (Vp and attenuation) have been made (Figure 4).

259 Due to the high resemblance between the attenuation profile and calcium oxide/calcite content at  
260 reference site GMCS05 (site 1 in Figure 1), both profiles have been plotted against each other (Figure  
261 5). With a regression coefficient  $R^2$  of around 0.9, values of attenuation and calcium oxide/calcite  
262 follow a linear trend. This observation is important as it allowed determining calcite profiles at sites  
263 where XRF/XRD tests could have not been performed, mainly due to high disturbance of recovered  
264 cores in question, as shown in section 4.1.2.

265 However, in cases where the tested core was not disturbed, calcite profiles were determined either  
266 directly from XRD results or indirectly from XRF results using equation 2. For the quartz profile,  
267 values were considered constant and equal to the average quartz content (around 6%) in sediments  
268 from core GMCS05 (site 1 in Figure 1). The clay fraction is then calculated using the following  
269 equation:

$$270 \quad f_{clay} = 1 - f_{calcite} - f_{quartz} \quad (3)$$

271 This allowed estimating the concentration of GH at all sites where Vp profiles were available.

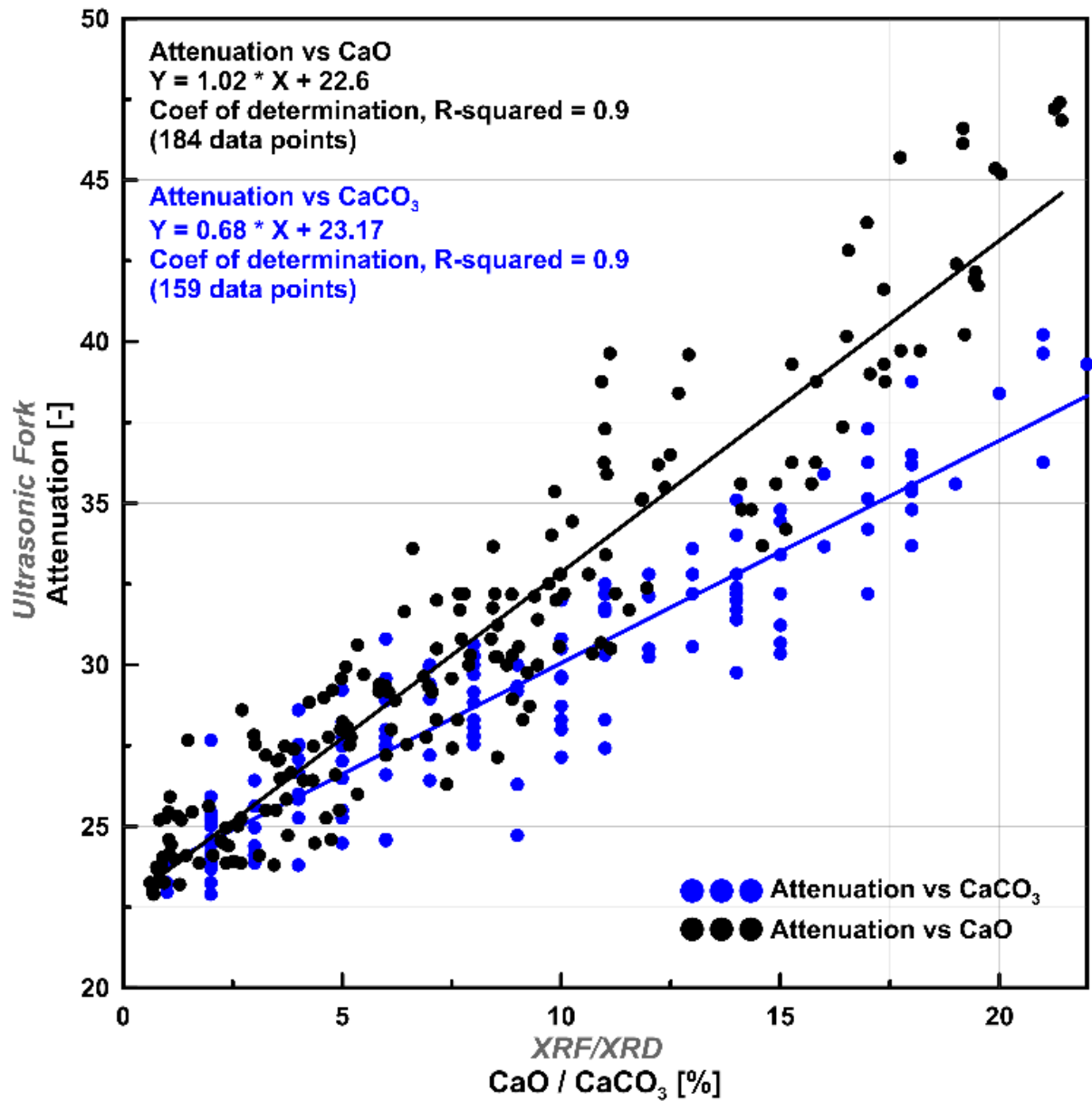


272

273 *Figure 4. Correlation between acoustic measurements for site GMCS05: a) compressional wave velocity and b) attenuation*

274 *and mineralogical composition: c) density, d) calcite (continuous black line) / calcium oxide (red crosses) and e) mineralogy*

275 *fractions (modified from Taleb et al. 2018).*



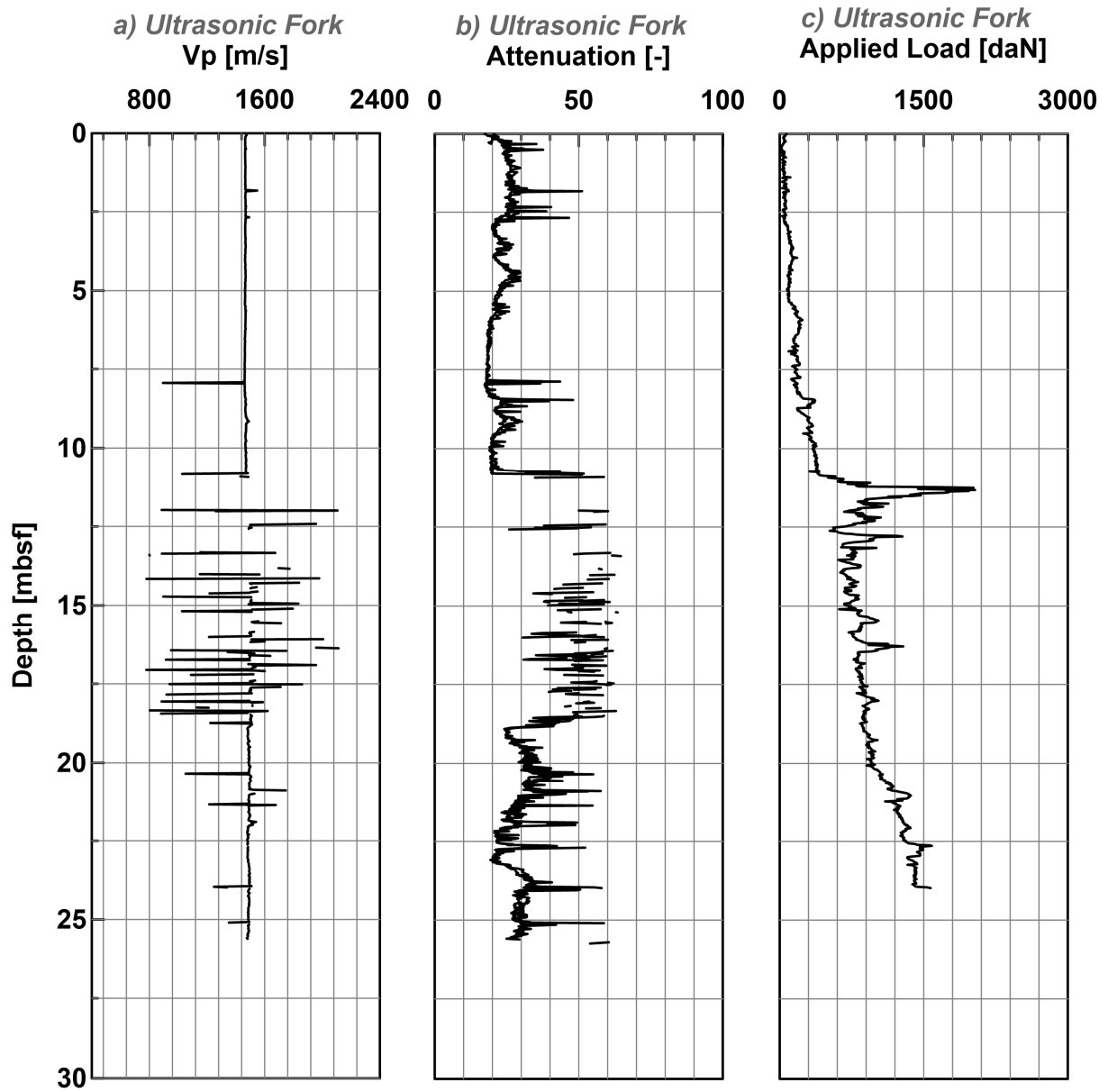
276

277 *Figure 5. Correlation of attenuation with calcium oxide and calcite fractions for core GMCS05*

278 4.1.2 Mineralogy derived from in-situ acoustic measurements

279 For some sites, XRF and XRD tests could not be carried out because of the absence of cores or the  
 280 disturbance of the sediment due to coring/drilling processes or GH dissociation upon core recovery.

281 The first step was to correlate all significant peaks and patterns of the in-situ compressional wave  
 282 velocity, the attenuation and the applied load profiles of the GH bearing site in question (Figure 6).



283

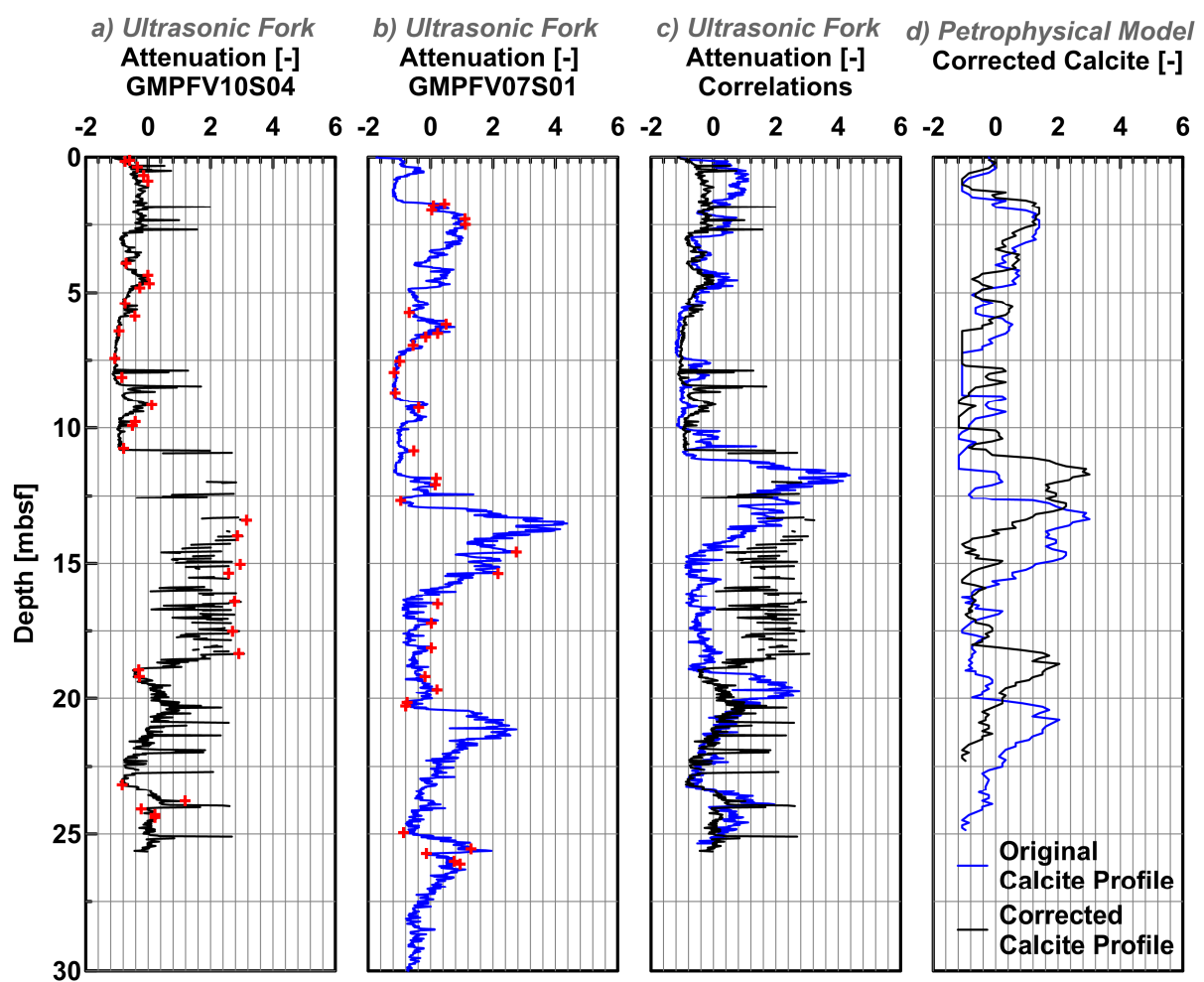
284 *Figure 6. GH bearing site GMPFV10S04 (site 4 in Figure 1) acquired by the ultrasonic fork: a) compressional wave velocity, b)*  
 285 *signal attenuation and c) applied load to penetrate the sediment.*

286 Based on earlier observations, the attenuation profile correlates best with that of calcite. Then, the  
 287 attenuation profile of the investigated site can be compared and correlated with that of a reference  
 288 site without GH, where XRF/XRD tests have been performed and the mineralogy profile determined.  
 289 To improve correlation between profiles, data have been first adimensionalised (Figure 7) using the  
 290 following equation:

291 
$$x = \frac{\bar{x} - x}{\sigma_x} \tag{4}$$

292 Where,  $x$  is the value that will be made dimensionless (i.e. attenuation, mineralogy profile),  $\bar{x}$  and  $\sigma_x$   
 293 are the mean and standard deviation values for  $x$ .

294 As represented in Figure 7.a and b (using red crosses), correlations were made by relating depths of  
 295 similar patterns in the attenuation profile of the reference and GH bearing sites. Then the adjusted  
 296 attenuation profile of the reference site (blue line in Figure 7.c) was superimposed on that of the  
 297 investigated site (black line in Figure 7.c). Eventually, the calcite profile was depth-adjusted with that  
 298 of the updated attenuation profile following the same process (Figure 7.d).



299  
 300 *Figure 7. Correlations between adimensionalised attenuation profiles of: a) GH bearing site GMPFV10S04, b) attenuation*  
 301 *profile of reference site GMPFV07S01, c) depth to depth correlation in terms of attenuation and d) adimensionalised original*  
 302 *calcite profile (blue continuous line) against adimensionalised depth-adjusted calcite profile (black continuous line) that*  
 303 *allow determining the mineralogy profile of GH bearing sediment at site GMPFV10S04 (blue curve in d).*

304 For the quartz profile, values were set to a constant that is equal to the average quartz content in the  
305 sediment (around 6%).The clay fraction is then calculated using equation 3.

306 Examples of other depth-adjusted attenuation profiles are provided in **Appendix A**. The residual  
307 error resulting from assumptions concerning the quartz profile is shown in **Appendix B**.

## 308 **4.2 Density Profile**

309 The density profile is a substantial parameter in the process of the Vp inversion to estimate GH  
310 content (Figure 4.c). It allows calculating the vertical effective stress and porosity, which in turn are  
311 key parameters for the mathematical and physical equations used to calculate the content of GH in  
312 the sediment. The density profile of core GMCS05 (Figure 4.c) was used to define the reference  
313 compression index ( $C_c$ ) and the initial void ratio ( $e_0$ ) needed to determine the evolution of the void  
314 ratio (or porosity) with effective stress using the following equation:

$$315 \quad e = e_0 - C_c \cdot \log \frac{\sigma'_v}{\sigma'_{v0}} \quad (5)$$

316 Where  $\sigma'_v$  is the vertical effective stress at a given level below the seabed and  $\sigma'_{v0}$  is a reference  
317 vertical effective stress taken equal to 1 kPa

318 From the density profile of GMCS05, values of 2.5 and 9.8 were estimated for  $C_c$  and  $e_0$  respectively.  
319 They were considered as representative only for the first 30mbsf of sediment. These values were  
320 used to calculate the porosity and hence the bulk density for each site. The sediment bulk density  
321 ( $\rho_b$ ) in this model is calculated as follows:

$$322 \quad \rho_b = \phi \rho_w + (1 - \phi) \rho_s \quad (6)$$

323 where,  $\rho_w$  is the water density

$$324 \quad \rho_s \text{ is the solid phase density: } \rho_s = \sum_{i=1}^m f_i \rho_i \quad (7)$$

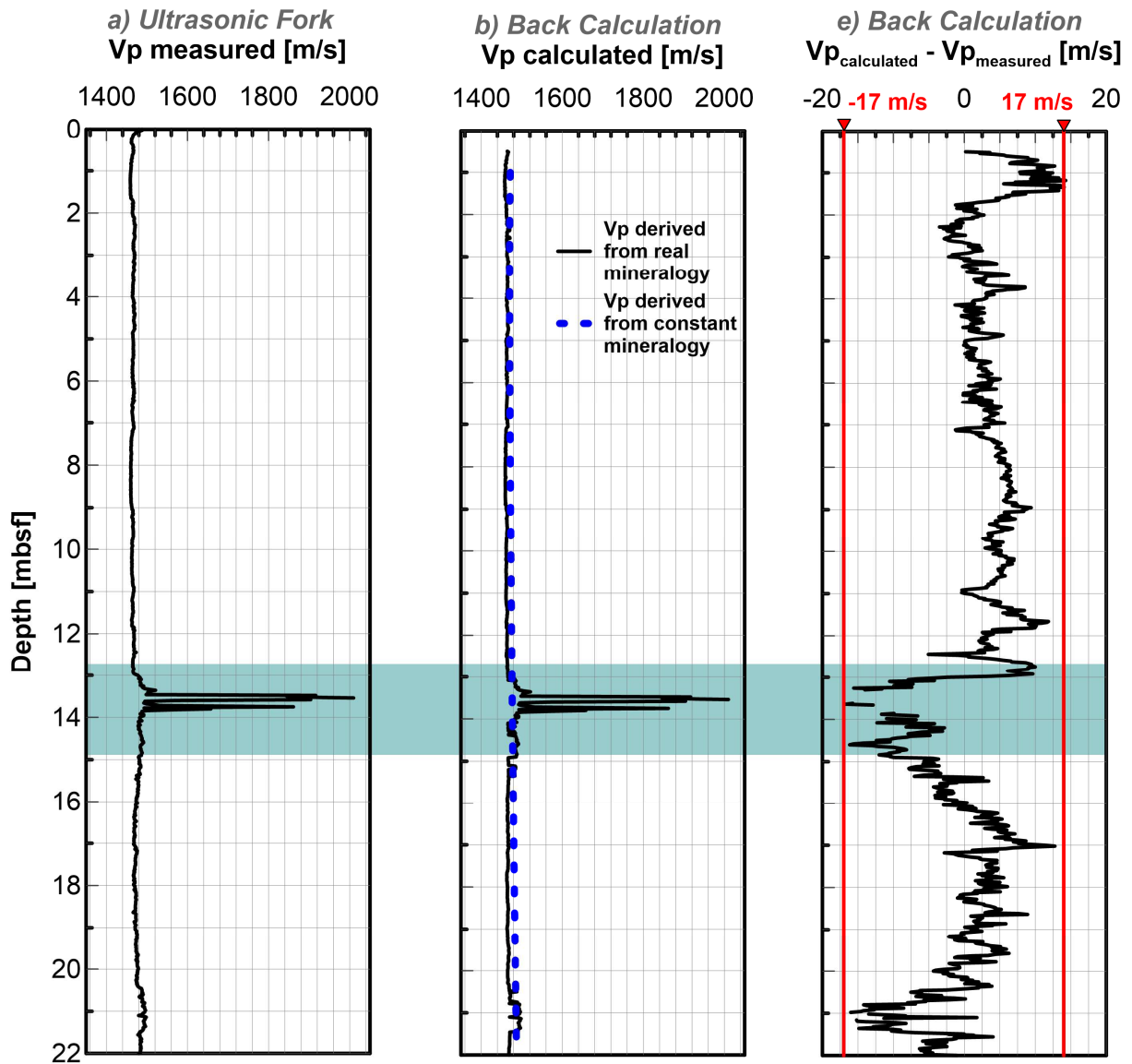
325  $f_i$  and  $\rho_i$  are the clay, calcite and quartz fractions and solid densities respectively.

326 The residual error resulting from the estimation of for  $C_c$  and  $e_0$  is shown in **Appendix B**.

### 327 4.3 Back-calculation for GH content

#### 328 4.3.1 For reference site (no GH)

329 The GMPFV07S01 is a Penfeld Vp reference site at which neither GH nor free gas were detected.  
330 Based on [Figure 8.a](#), reference sites are characterised by Vp oscillating between 1450 m/s and 1510  
331 m/s; however, a clear peak of 2015 m/s is noticed at around 13.6 mbsf (blue rectangular zone in  
332 [Figure 8](#)). Such peak was related to the presence of foraminifera in the sediment ([Figure 2](#)).  
333 Measured and calculated Vp are compared in [Figure 8.a](#) and [Figure 8.b](#) respectively. It can be  
334 observed that both profiles yield almost the same results, which proves the reliability of the EMT in  
335 reproducing the in-situ acoustic properties of the sediment.  
336 Moreover, in order to highlight the importance of the mineralogy profile with respect to the  
337 quantification process, a mean mineralogy profile with constant fractions of clay, calcite and quartz is  
338 proposed. The new profile constitutes of 80.5% clay, 12.6% calcite and 6.9% quartz, which are the  
339 average values of each fraction respectively. The blue dashed line in [Figure 8.b](#) shows the calculated  
340 Vp profile derived from the new constant mineralogy profile, which oscillates around 1464 m/s and  
341 1483 m/s. These values do not represent the real measured values from the Ultrasonic fork ([black](#)  
342 [continuous line in Figure 2.b](#)); hence, GH contents derived from such values will not be realistic nor  
343 representative of the sediment in question. Indeed mineralogical variations of the core are essential  
344 to capture its acoustic response, which is the main element in the quantification process of GH [Kim et](#)  
345 [al. \(2013\)](#).  
346 Additionally, to narrow down the calculation errors that could occur during the quantification  
347 process, the difference between the velocity calculated by the model and the measured velocity was  
348 calculated and found to oscillate in the range  $\pm 17$  m/s. Hence, GH contents will only be determined  
349 when the difference between the calculated and measured Vp is greater than 17m/s.



350

351 *Figure 8. Reference site GMPFV07S01 (site 1 in Figure 1): a) Vp measured using in-situ tool, b) Vp calculated using effective*  
 352 *medium theory based on real (continuous black line) and constant (dotted blue line) mineralogy and c) difference between*  
 353 *calculated velocity and measured velocity (Modified from Taleb et al. 2018).*

354 4.3.2 For sediment with GH

355 GH were quantified at all sites where Vp data were available and after definition of the mineralogy  
 356 profile of the sediment in question, which was mostly done by correlating acoustic data (attenuation  
 357 profile) of GH bearing sites with that of reference sites. This is because, in most cases, recovered  
 358 cores from GH bearing sites are highly disturbed due to GH dissociation during their recovery.

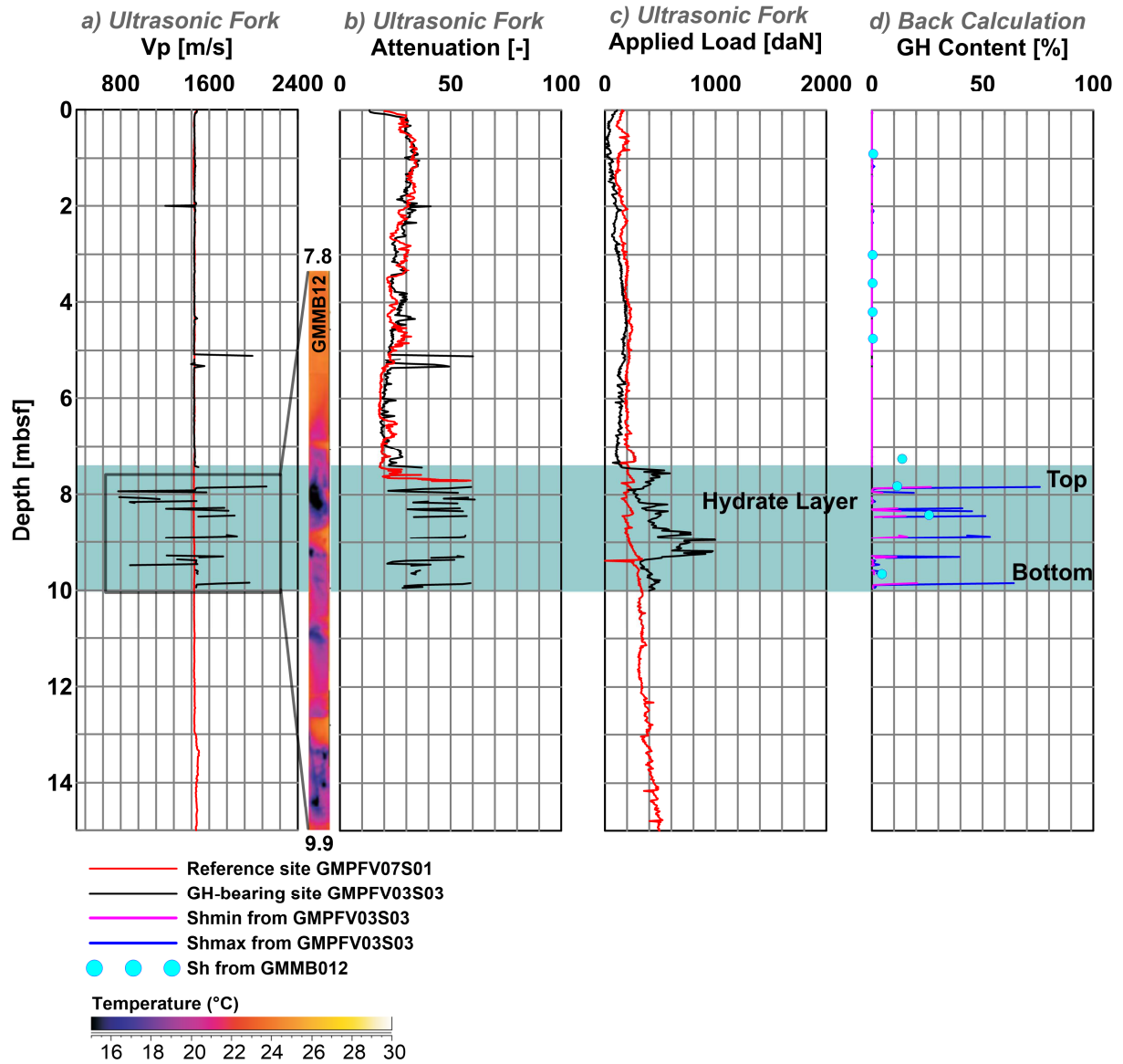
359 Quantification results obtained from the EMT were compared to pore-water chloride analysis and  
360 pictures of nearby recovered cores, which allowed carrying out a more reliable investigation of GH  
361 bearing sediments.

362 Figure 9 presents the Vp, the signal attenuation and the applied load at site GMPFV03S03 (site 2 in  
363 Figure 1). The positive and simultaneous increases of all three parameters confirms the presence of  
364 GH at this site. On the other hand, negative Vp anomalies indicate the presence of free gas within  
365 the sediment; thus, allowing determining layers where solid hydrate and free gas coexist.

366 At 7.5 mbsf, missing data in the Vp and signal attenuation profiles correlates with an increase of  
367 around 560 daN of the applied load, which suggests that GH were touched at this depth. This is  
368 followed by sudden increases of up to 2131 m/s in Vp and 60 in the signal attenuation at 7.8 mbsf.  
369 These results have been compared to infrared thermal scanning performed by *Wei et al. (2015)*. The  
370 temperature

371 measurements that can be performed by the IR camera range from  $-40^{\circ}\text{C}$  to  $+120^{\circ}\text{C}$  with an  
372 accuracy of  $\pm 2^{\circ}\text{C}$ . The difference between the surface temperature and the background temperature  
373 has been calculated in order to analyse the recovered core (*Wei et al., 2015*). Anomalies higher than  
374  $1^{\circ}\text{C}$  are interpreted as voids in the recovered core, while anomalies lower than  $-2^{\circ}\text{C}$  were considered  
375 as indicative of the presence of GH. Nearby core GMMB12 (*Wei et al., 2015*) revealed temperatures  
376 as low as  $16^{\circ}\text{C}$ , which is due to the endothermic dissociation of GH. These colder temperatures,  
377 compared to reference sediments, indeed confirm the presence of GH. The recovery of these cores  
378 promote GH dissociation and therefore gas release and sediment expansion, which can lead to  
379 sediment expulsion from the core section. At this stage, it is important to mention that MeBo cores  
380 are composed of 1.50 m long sections. Therefore, the case of sediment expulsion and the depth  
381 accuracy of the hydrate recovered thanks to the MeBo is limited by the section length. It is then  
382 reasonable to consider this IR method as an extra and qualitative means to confirm the presence of  
383 GH.

384 The GH contents estimated with the EMT were averaged over depth intervals of 10 cm and then  
 385 compared to those obtained from pore-water chloride analyses. Using Vp data, maximum GH  
 386 contents were estimated to occur at 7.85 mbsf with values of 27% for  $S_{hmin}$ , 76% for  $S_{hmax}$  while a  
 387 lower value of 11.5% was estimated by using the pore-water chloride data.

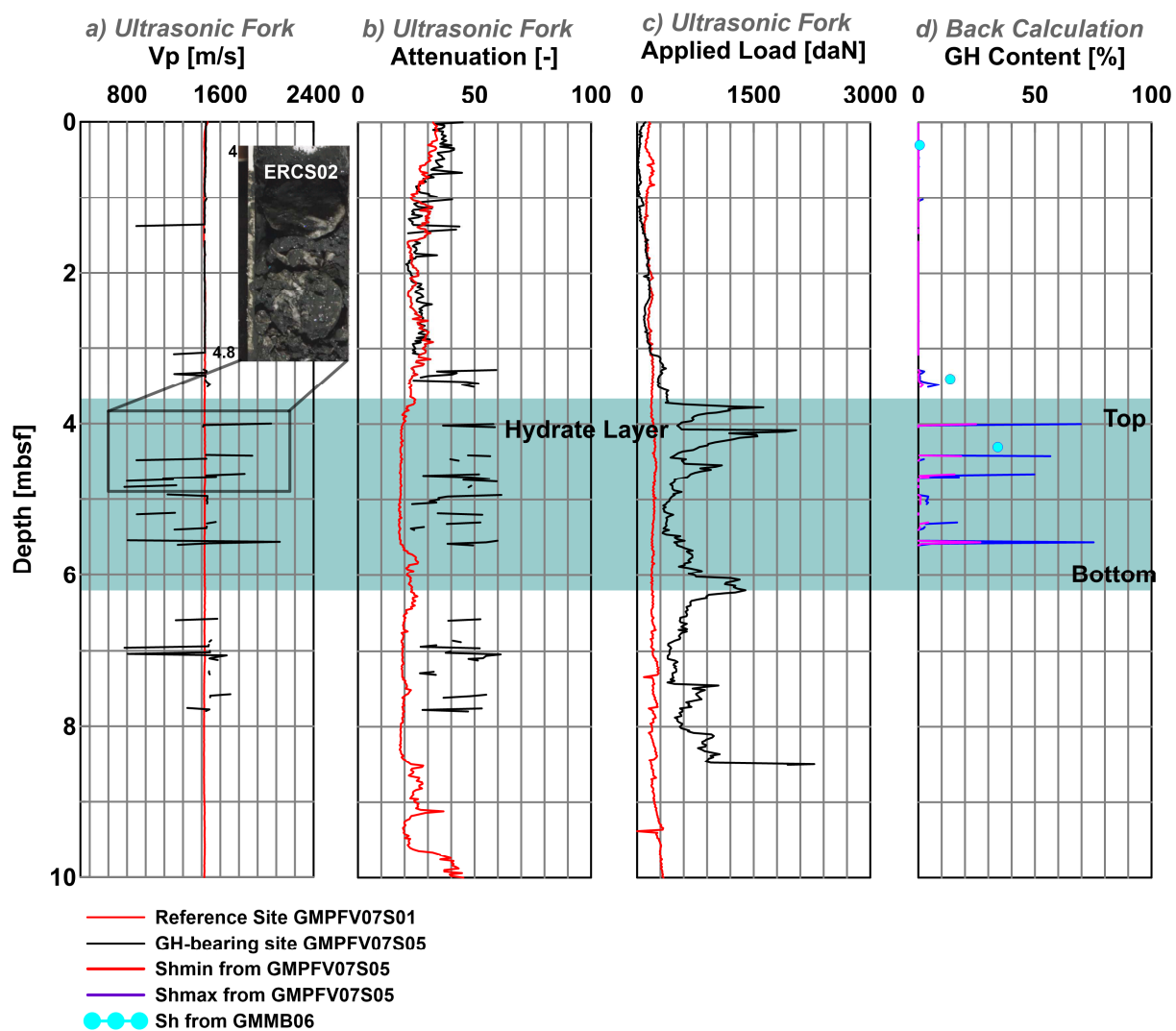


388

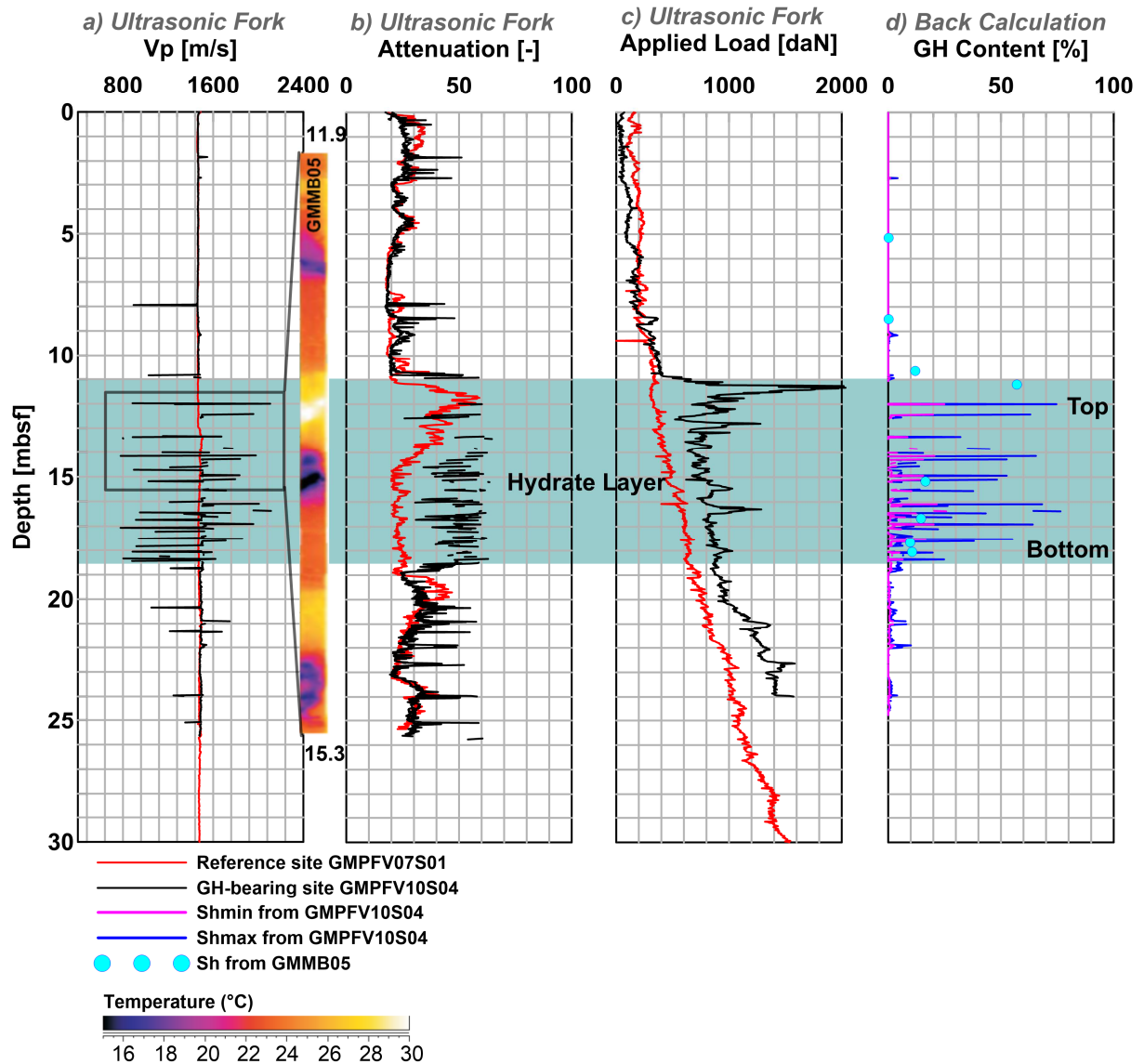
389 *Figure 9. a) P-wave velocity, b) depth-adjusted attenuation profile, c) applied load for site GMPFV03S03 (black curves)*  
 390 *against reference site GMPFV07S01 (blue curves) and d) GH content for site GMPFV03S03 (modified from Taleb et al. 2018).*

391 For the GMPFV07S05 site shown in Figure 10 (site 3 in Figure 1) an abrupt increase in the applied  
 392 load (1633 daN) at around 3.8 mbsf followed by a strong increase in Vp and signal attenuation (2050

393 m/s and 58 respectively) at 4 mbsf were observed. These values are up to 2 times higher than those  
 394 obtained at the reference site at the same depths, which indicates the presence of GH. Additionally,  
 395 photos of nearby Calypso core CS02 showed the presence of massive GH nodules followed by a 30  
 396 cm thick interval containing GH veins (Figure 10). Using the EMT, maximum GH content were  
 397 estimated to occur at 4mbsf with values of 25% for  $S_{hmin}$  and 70% for  $S_{hmax}$ . At 4.3 mbsf, the GH  
 398 content estimated from chloride concentration anomalies measured on MeBo core GMMB06  
 399 reaches 34%.



401 Figure 10. a) P-wave velocity, b) depth-adjusted attenuation profile, c) applied load for site GMPFV07S05 (black curves)  
 402 against reference site GMPFV07S01 (blue curves) and d) GH content for site GMPFV07S05



403

404 *Figure 11. a) P-wave velocity, b) depth-adjusted attenuation profile, c) applied load for site GMPFV010S04 (black curves)*

405 *against reference site GMPFV07S01 (blue curves) and d) GH content for site GMPFV10S04*

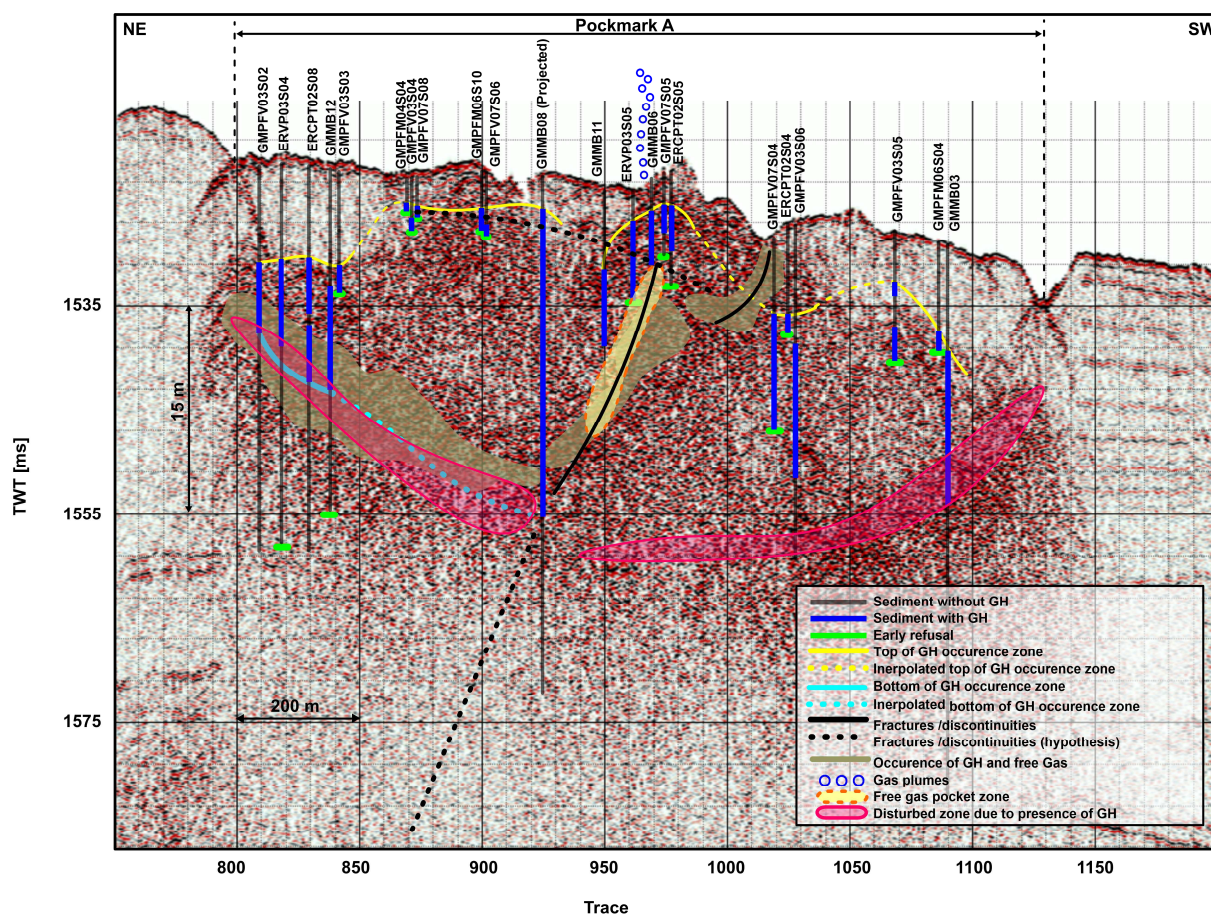
406 **Figure 11** presents the  $V_p$ , the signal attenuation and applied load profiles obtained at site  
 407 GMPFV10S04 together with estimates of GH content (site 4 in Figure 1). The presence of GH can be  
 408 confirmed due to simultaneous increases of in-situ acoustic parameters (**Figure 11**) and negative  
 409 thermal anomalies of the nearby core GMMB12 (Wei et al., 2015).

410 While missing data is observed in the P-wave velocity and attenuation profiles between 11 mbsf and  
 411 12 mbsf, the applied load profile suggests that GH were touched at 11 mbsf. This was confirmed by  
 412 the pore-water chloride data from which GH content as high as 57.5% was estimated to occur at 11.2

413 mbsf. This is followed by abrupt increases of 2111.2 m/s in  $V_p$  and 60 in signal attenuation, which  
 414 highlights the effect of the presence of GH within the sediment. Maximum GH contents were found  
 415 to occur at 12 mbsf with values of 20.5% for  $S_{hmin}$  and 75.6% for  $S_{hmax}$ .

416 Following previous work in *Taleb et al. (2018)*, GH contents derived from the EMT were compared  
 417 with those derived from the pore-water chloride analysis. This showed that estimates of GH contents  
 418 relying on the assumption that hydrate contributes to the stiffness of the sediment by becoming part  
 419 of the load-bearing framework ( $S_{hmin}$ ) are closer to those obtained from the chlorinity data. Hence,  
 420 in the rest of this work only  $S_{hmin}$  (referred to  $S_h$  in the following) values will be considered and  
 421 discussed.

#### 422 4.4 Correlation between estimates GH content and seismic signatures



423  
 424 *Figure 12. Seismic profile SY03-HR-Pr01 showing a marked contrast between the high-amplitude chaotic facies in the central*  
 425 *part of pockmark A and the continuous sub-parallel facies of the surrounding sediments. Blue hollow circles indicate the flow*  
 426 *path of free gas visually observed during drilling at site GMMB06.*

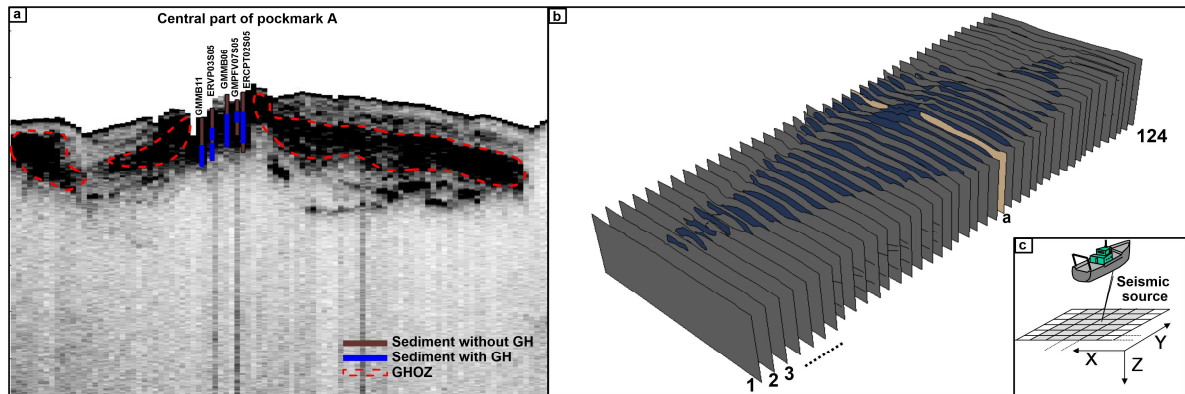
427 As shown in Figure 1 and Figure 12, a number of in-situ measurements and cores can be tied to  
428 seismic profile SY03-HR-Pr01 in order to analyse the larger scale distribution and morphology of GH  
429 present within pockmark A and define the top and in some cases the bottom of the GHZ.

430 In Figure 12 a significant contrast is observed between the high-amplitude chaotic facies in the  
431 central part of pockmark A and the continuous facies of low-amplitude sub parallel reflectors outside  
432 of its peripheral depression. In most zones, the top of the high-amplitude chaotic facies is observed  
433 to correlate with the top of GHZ as inferred from the analysis of in-situ and core data (yellow  
434 continuous line in Figure 12). Delineating the base of GHZ proved much more difficult since at  
435 almost all sites early refusals were met during acoustic soundings (green segments in Figure 12).  
436 Early refusals suggest that the top of a second GH layer has been probably reached. The depths at  
437 which they occurred generally correlate with the presence of chaotic facies of higher energy on  
438 seismic profile SY03-HR-Pr01. These observations were found to almost correlate with the GH and  
439 free gas occurrence zones (light green zones on Figure 12) proposed by *Sultan et al. (2014)*.

440 On both sides of the profile, disturbed zones attributed to the presence of GH were highlighted (pink  
441 zones on Figure 12). They correspond to the top of a curved-shaped succession of hyperbolae  
442 interpreted as a zone of fractures/discontinuities suspected by *Sultan et al. (2014)*. In the central part  
443 of the NE-SW seismic profile (Figure 12), it is possible to identify the presence of  
444 fractures/discontinuities (solid black lines in Figure 12). These fractures are thought to be  
445 preferential paths for the free gas migration throughout the pockmark. This is further confirmed by  
446 this study based on visual observation of gas plumes at the centre of the pockmark (blue bubbles on  
447 Figure 12) and by the free gas pocket zone (light orange zone on Figure 12), which was discovered  
448 upon drilling at core GMMB11.

449 Alternatively, a total of 103 sub-bottom profiles in the x-axis direction and 124 in the y-axis direction  
450 were acquired from the C&C AUV survey within pockmark A (*George and Cauquil, 2007*). In Figure  
451 13.a, five sites (GMMB11, ERVP0305, GMMB06, GMPFV07S05 and ERCPT02S05) were projected on a  
452 seismic profile passing through the central part of pockmark A. It can be observed that the presence

453 of GH as inferred from in-situ and laboratory measurements correlates well with the high-amplitude  
454 chaotic facies (dark zones in Figure 13), in a way such that the surrounding low amplitude to  
455 transparent facies (grey areas on Figure 13) is thought to be indicative of the absence of GH in  
456 sediments. All profiles were then analysed and used (Figure 13.b) to create a 3D seismic data cube  
457 and identify the GHZO throughout pockmark A.



458  
459 *Figure 13. a) Seismic profile through the central part of pockmark A showing a sharp contrast between a high-amplitude*  
460 *chaotic facies (black zones) and a low-amplitude to transparent facies (grey areas), b) Seismic profiles in y-axis direction*  
461 *interpreted in order to create a 3D seismic data cube and c) illustration showing the directions in which the seismic profiles*  
462 *have been made.*

## 463 5. Discussion

### 464 5.1 GH detection and quantification

465 In this paper, GH contents have been estimated from in-situ  $V_p$  measurements as well as from  
466 pore water chloride analyses carried out on adjacent cores. The presence of GH in clayey  
467 sediments was inferred from increases in P-wave velocity as well as from negative anomalies in  
468 the chlorinity and temperature profiles. Furthermore, positive anomalies in the attenuation and  
469 applied load profiles were also taken as an indicator of the presence of GH.

470 The quantification process required the use of a petrophysical model allowing sites lacking  
471 mineralogical input data to be correlated with reference sites, where background velocity

472 profiles and mineralogy are well defined. Using the EMT, a maximum GH content of 26.5%  $S_{hmin}$   
473 was estimated at a Vp of 2035 m/s.

474 It is arguable that relying on the assumption that GH contribute to the stiffness of their host  
475 sediment is not suitable for the case of clayey sediments, which is characterised by the presence  
476 of grain-displacing hydrates. Based on a comparative study conducted by Ghosh et al. (2010), the  
477 method where GH are assumed to contribute to the stiffness of their host sediment ( $S_{hmin}$  in  
478 this study) overestimates GH content by 7-11% with respect to the pressure coring method. Even  
479 though the method proposed by *Ghosh et al. (2010)* to account for the grain-displacive  
480 morphology is arguably the most accurate to quantify GH in clayey sediments, it could not be  
481 used in this work due to a lack of quantification of the precise geometry and orientation of GH  
482 within the sediment.

483 *(Shankar et al., 2013)* used the EMT to determine GH and free gas saturation in the Krishna-  
484 Godavari Basin, eastern Indian margin. The basin is dominated by clayey sediments and it was  
485 reported that GH occurred in fractures as veins or nodules. Numerical results have shown that  
486 the effective medium models are more accurate compared with tested empirical models, since  
487 the physical properties of the sediment were taken into consideration. *Lee and Collett. (2009)*  
488 compared different GH estimation methods to the pressure core one while trying to account for  
489 fracture orientation within the sediments. GH estimates derived from elastic velocities while  
490 assuming high presence of angle fractures correlate well with the pressure coring method.  
491 However, results have shown that the effect of fractures on GH content derived from electrical  
492 resistivity and S-wave velocity is greater compared to values derived from P-wave velocity.

493 Furthermore, velocity-derived estimates of GH were compared to those derived from pore-water  
494 chloride anomalies to evaluate the reliability of both upper and lower bound GH content.  
495 Estimates assuming a load bearing contribution of hydrate to the mineral framework ( $S_{hmin}$ )  
496 were found to match better with the results derived from the chloride concentration anomalies

497 in pore water (*Taleb et al., 2018*). Based on all these arguments, it was reasonable to consider  
498  $S_{hmin}$  as the most representative of GH content in the study area.

499 On the other hand, one might argue that the pore-water chloride analysis can be associated with  
500 calculation uncertainties. Such method has been used in many research works (*Ussler and Paull,*  
501 *2001; Torres et al. 2004; Riedel et al., 2005 and Riedel et al., 2006*). Variables in equation 1 such  
502 as  $C_{cb}$  has been often considered as a limitation for this method.  $C_{cb}$  might be affected by the in-  
503 situ high pore fluid salinity caused by rapid GH formation or by in-situ low salinity caused by GH  
504 dissociation. At this stage, it is challenging to define an uncertainty range of  $C_{cb}$  in the case of the  
505 present work. However, *Riedel et al. (2006)* proposed a  $\pm 0.5$  (of standard deviation unit) range  
506 of uncertainty for  $C_{cb}$ . This range has been determined based on works performed by *Ussler and*  
507 *Paull (2001)* and *Torres et al. (2004)*. Moreover, *Joshi et al. (2018)* performed a study aiming at  
508 estimating GH saturation in the Krishna Godavari Basin. The authors derived GH content from  
509 measured and modelled velocities, which were later compared to GH content derived from  
510 pressure coring and chlorinity analysis. Results have shown that GH from chlorinity analysis as  
511 well as from pressure coring match well with those derived from the velocity inversion method.  
512 *Wang et al. (2011)* compared results derived from EMT, while assuming GH as component of the  
513 solid phase, to those derived from chlorinity analysis. The depth intervals at which GH occurred  
514 were found similar in the case of both methods. Therefore, validating the comparative approach  
515 between different GH quantifying methods adopted in this paper.

516 Additionally, the distribution of GH within the study area has been discussed by *Wei et al. (2015)*  
517 based on negative thermal anomalies obtained from infrared imaging results. Looking at Figure 9  
518 and Figure 11, it can be seen that the GHZOZ determined by *Wei et al. (2015)* correlates well with  
519 that derived from EMT. This confirms that the presence of GH can be detected and quantified  
520 based on positive Vp anomalies.

521 Another limitation to the quantification of GH based on in-situ acoustic measurements is that the  
522 device used can detect compressional wave velocities only up to 2200 m/s. This has implications

523 especially where massive GH nodules were observed within the recovered cores between two  
524 layers of sediments. Based on laboratory analyses, one may indeed expect the Vp to increase to  
525 values higher than 3000 m/s in the presence of such massive GH nodules (*Helgerud et al., 2009*).

526 This could explain the discontinuities in the Vp profiles which precluded the exhaustive of GH.

527 One more constraint affecting the quantification of hydrates is the coexistence of free gas, which  
528 is known to decrease Vp (*Helgerud et al., 1999*). Because the effective medium model used solve  
529 equations with GH and free gas as two independent variables the actual GH content might have  
530 been locally underestimated.

### 531 **5.2 3D model of pockmark A: seabed morphology versus hydrate/fluid distribution**

532 *Sultan et al. (2014)* and *Wei et al. (2015)* have identified the different formation stages of the  
533 pockmarks within the study area, which is marked by a the presence of a graben bordered by  
534 deep seated faults through which gas migrates (*Marsset et al., 2018*). The continuous supply of  
535 upward migrating gas has been considered as efficient enough to reopen sealed fractures or  
536 even create new ones. This would have promoted GH hydrate formation and consequent  
537 decreases in pore space and permeability. Such a situation is expected to have favored the  
538 development of overpressures and in turn that of new fractures/discontinuities.

539 *Dewangan er al. (2010)* investigated the seabed morphology and gas venting features in the  
540 region of Krishna-Godavari basin, where the presence of GH has been proved based on drilling  
541 and coring results (*Collett et al., 2008*). According to *Bastia (2006)* the Krishna Godavari basin  
542 has similar geological features as those described by *Damuth (1994)* for the Nigerian continental  
543 margin. The area was observed to be characterised by several subsurface mounds, acoustic voids  
544 and acoustic chimneys, which were related to fluid/gas upward movements. This has led to the  
545 formation of muliple fractures and hence promoted accumulations of GH in the Krishna Godavari  
546 region similar to those found in the present study area (*Brooks et al., 2000*).

547 Moreover, *Dewangan et al. (2010)* and *Riedel et al. (2010)* have discussed that the presence of  
548 faults in an area controls the distribution of GH accumulations, particularly the fracture filling  
549 type. *Gullapalli et al. (2019)*, investigated this fact by studying the implications of free gas  
550 migration on accumulations of GH using seismic data. Results have shown that free gas is  
551 migrating within the GH stability zone and promoting shallow GH accumulations. Such  
552 observations have been also previously reported by *Wood et al. (2002)* based on analysis of  
553 seismic data in the Cascadia margin, Canada.

554 In order to investigate the effect of the presence and distribution of GH on the geomorphology of  
555 the present pockmark, AUV seismic profiles through pockmark A (*George and Cauquil, 2007*)  
556 were used to illustrate the detailed architecture of GHZO inside the pockmark. This eventually  
557 allowed calculating the GHZO volume and its occupancy ratio in pockmark A ([Figure 14](#)).

558 In between the top and base of the GHZO some intervals were delineated as zones where GH are  
559 absent. These so-called “GH free intervals” show three different shapes (A, B and C in [Figure 14](#)).  
560 By assuming that both GHZO and the “GH free intervals” have an ellipsoidal shape, the total  
561 volume occupied by GH-bearing sediments was estimated to be on the order of  $2.7 \times 10^6 m^3$ .  
562 Then, the GH volume was calculated by considering a mean hydrate fraction of 21%, which is the  
563 mean of all highest GH content at each site in pockmark A. This value is in accordance with  
564 results from *Sultan et al. (2007)* where GH content from 3D seismic data was found to be equal  
565 to 20% in pockmark A. Therefore, the GH volume was found equal to  $0.57 \times 10^6 m^3$ . The total  
566 volume of the pockmark was estimated in order to determine the total occupancy of GH. Based  
567 on seismic data, pockmark A was assumed to extend down to 45 m below seafloor. Accordingly,  
568 GHZO was found to occupy 17% of the total pockmark volume with a GH volume equivalent  
569 to  $0.57 \times 10^6 m^3$ . It is debatable that such calculations might be outdated due to rapid  
570 formation and dissociation of GH in the study area. However, such mechanisms are localised in  
571 the shallow central part of the pockmark, which is only a small volume compared to the whole

572 pockmark. *Bayon et al. (2015)* carried out Uranium-Thorium dating on a carbonate-rich layer of a  
573 sediment recovered from the study area. Results have shown that carbonate precipitation  
574 related to intense fluid seepage has occurred between 13 and 10 ka. This proves that the present  
575 hydrate-pockmark is evolving since thousands of years.

576 Furthermore, two sections (NE-NW and SW-SE) were extracted from the 3D bathymetry ([Figure](#)  
577 [15](#)). On both sections, seismic profiles were projected as well as GH contents from in-situ data  
578 and the GHOZ (blue zones in [Figure 15](#)) as outlined in [Figure 14](#). These correlations indeed  
579 highlight the heterogeneous distribution of solid hydrate and free gas within the pockmark,  
580 which is an observation already reported by many authors in different GH-rich region (*see for*  
581 *instance Wang et al., 2011*). Finally based on all these observations and analyses, a detailed  
582 description of the actual fluid/hydrate dynamic distribution within the pockmark can be  
583 proposed. The highest GH contents (20%-30%) are observed to be in the centre while lower  
584 contents (0%-10%) are mostly observed at the borders of the pockmark. This is in line with the  
585 actual morphology of the pockmark showing mostly bumps in the central part due to high  
586 content of GH and a slight depression on the borders where according to *Sultan et al. (2010)* GH  
587 might have dissolved. At this stage, it is interesting to note core GMMB08 (site11 in [Figure 15.a](#))  
588 has been projected from a distance of 86 m, which explains why it intersects GH free intervals .

589 It is also noteworthy that the GH and free gas occurrence zones cover all the proposed  
590 fractures/discontinuities and disturbed zones shown in pink in [Figure 12](#). *Taleb et al. (2018)*  
591 discussed the presence of GH having a spongy texture in the study area (light green zones in  
592 [Figure 15](#)) due to free gas being trapped within the pores of GH itself. This is due to the high gas  
593 flux present in the study area, which stimulates rapid GH formation; hence, causing the  
594 coexistence of both phases. In other cases, GH forms on the inner walls of the  
595 fractures/discontinuities, which isolate free gas from the surrounding pore water (yellow zone in  
596 [Figure 15.a](#)).

597 A bump can be observed at sites ERCPT02S05, GMPFV07S05 and GMMB06 (site 25, 26 and 27 in  
598 [Figure 15.b](#)). This is interesting since this location accommodates shallow GH with different  
599 morphologies (*Taleb et al. 2018*) such as massive nodules or thin veins (direct visual observations  
600 of core ERCS02 in Figure 10) as well as gas plumes at site GMMB06 (blue bubbles on [Figure 12](#)).  
601 Free gas might be escaping through fractures within the sediment and contributing to further  
602 shallow GH formation. These fracture zones have preferentially near-vertical orientations and  
603 contribute to the continuous supply of free gas, which in turn contributes to maintaining the  
604 presence of GH. Therefore, the bulge at this location might be formed to accommodate new GH  
605 formations and already existing high GH content. In other words, the shallowest GH  
606 accumulations in the pockmark are directly related to a central fracture or set of fractures that is  
607 supplying gas up to the water column. Lateral gas migration away from the central fracture,  
608 circulating from the highest to the lowest free gas/GH contents, is thought of as the most likely  
609 factor to explain why the shallow hydrate accumulation in the central part appears to follow the  
610 same geological horizons ([Figure 13](#)). All the processes here proposed would be directly or  
611 indirectly related to the vigorous gas flux through the central part of the pockmark as confirmed  
612 by the gas plumes in the water column and the free gas pocket zone (yellow line in [Figure 15](#)).

613 Thinner and deeper GH accumulations are generally observed in the peripheral depression of the  
614 pockmark ([Figure 12](#) and sites 17 and 18 in [Figure 15.a](#)). This can be explained by the fact that GH  
615 in this part of the pockmark have already disappeared probably due to a dissolution process as  
616 described by *Sultan et al. (2014)* and to initially lower GH contents there as observed in [Figure](#)  
617 [15](#). Such phenomena is not considered to be caused by dissociation because at this depth  
618 stability conditions (low temperature and high pressure) for GH formation are respected.

619 These observations are in line with seismic characteristics discussed by *Kumar et al. (2019)* in  
620 order to detect the presence of solid GH and free gas. According to *Chand and Minshull (2003)*,  
621 many seismic features can highlight the presence of GH and/or free gas, such as blanking and

622 vertical acoustic wipeouts. The latter has been reported by *Bouriak et al. (2000)* in the Storegga  
623 slide area and has been related to upward fluid migration. *Judd and Hovland (2009)* indicated  
624 that the escape of fluids to the seafloor is an important factor in pockmark formation that can be  
625 mapped using seismic and bathymetry data. Furthermore, this migration does not only consist of  
626 gas moving upward but also of heat, which can contribute to localised GH dissociation (*Chand*  
627 *and Minshull, 2003*).

628 At this stage, a comparison between pockmark A and other pockmarks, highlighting the  
629 similarities and differences, is interesting in order to further understand the geological features  
630 of the study area. *Hovland and Svensen, (2006)* and *Vaular et al. (2010)* have performed studies  
631 on the Nyegga pockmark in the mid-Norwegian margin, where the presence of GH has been  
632 confirmed. The authors have proposed several stages that can promote GH formation: high gas  
633 flux up to the seafloor and thermobaric conditions corresponding to the stability conditions of  
634 GH. Similarly to pockmark A, the gas flux through the seafloor of the Nyegga pockmark is  
635 heterogeneously distributed and GH forms where the flux is highest and in contact with water.  
636 After comparing pockmarks A and C with that of the Nyegga region, it can be observed that they  
637 share comparable dynamics: the morphology of the pockmark grows and collapses over time due  
638 to cycles of formation and dissociation/dissolution of GH in the shallow sub-surface sediment. On  
639 the other hand, *Sahling et al. (2008)* have studied three morphologically complex pockmarks (the  
640 Kouilou pockmarks) in the northern Congo Fan area, where they proved the presence of a 25-30  
641 m thick shallow GH layer. By contrast with that of the study area, pockmarks in Kouilou did not  
642 exhibit gas venting features. This suggests that pockmarks in the study area are probably more  
643 active with respect to free gas flux, compared to the Kouilou pockmarks; or that the last one is  
644 probably in an earlier phase of GH formation. Additionally, *Riboulot et al. (2016)* have correlated  
645 geophysical, sedimentological and geotechnical data in order to obtain insight into the inner  
646 architecture of pockmarks situated in the eastern Niger submarine delta. The study showed that  
647 the pathway through which the free gas is migrating and feeding the GHZOZ is located beneath

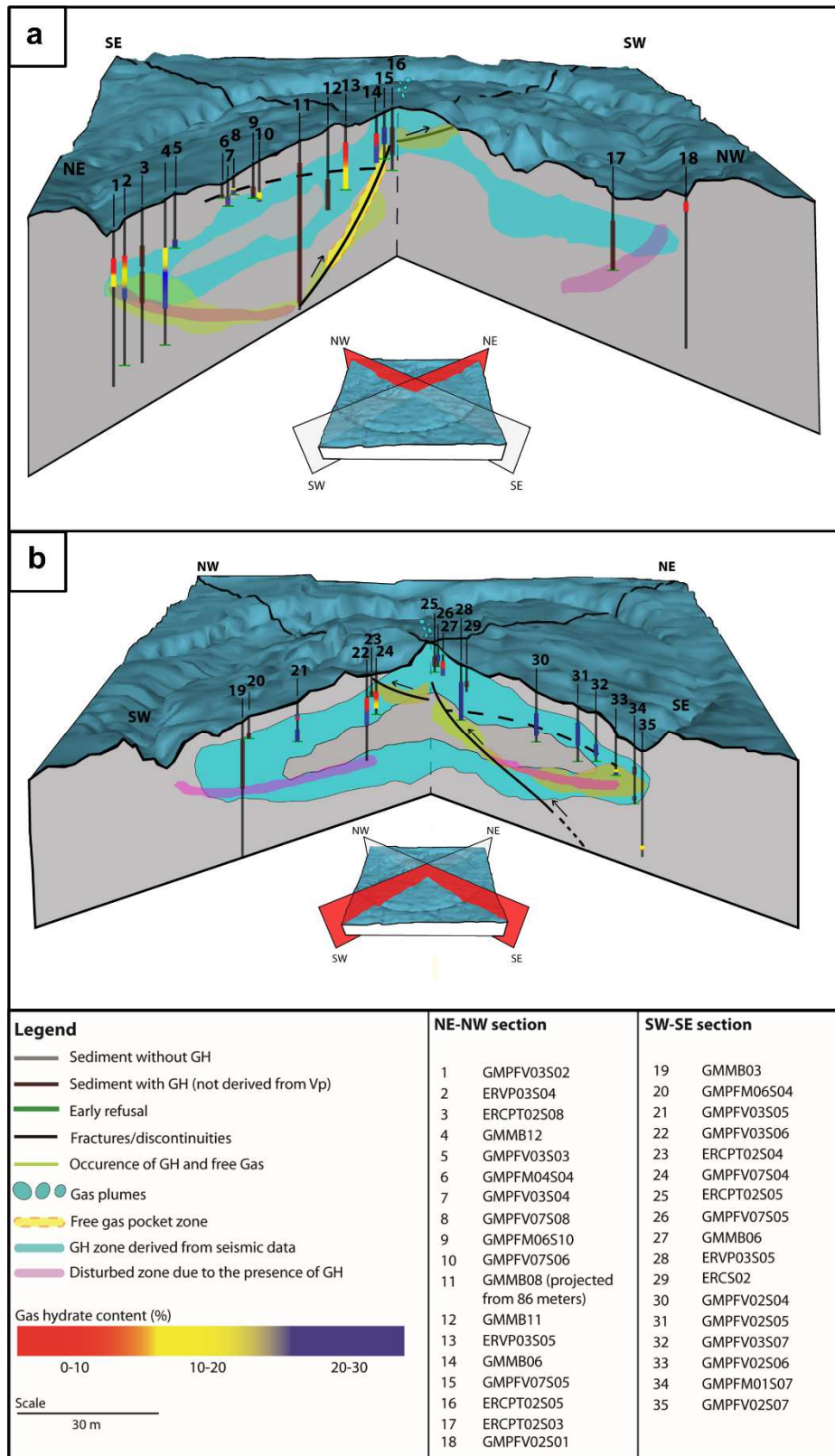
648 the central part of the studied pockmark. This is in line with this work, since the highest GH  
649 contents were identified in the central part of pockmark A (at sites 14, 15 and 16 in [Figure 15.a](#)  
650 and sites 25, 26 and 27 in [Figure 15.b](#)). Furthermore, the GHZOZ ([Figure 14](#)) has a similar geometry  
651 as the 3D bathymetry of pockmark A showing the influence of GH presence on the formation of  
652 the pockmark. All these findings confirm that GH content and distribution play an important role  
653 in shaping and forming of some pockmarks.

654 Therefore, complex seafloor morphologies, such as pockmarks, can be an indicator of the  
655 presence of GH ([Riboulot et al., 2016](#)) and must be considered as a potential source of geohazard  
656 particularly for industrial seabed developments (i.e. offshore operations, pipeline installations  
657 and well drilling). The correlations between in-situ acoustic and geotechnical measurements with  
658 the seismic data have indeed allowed understanding the link between the morphology of  
659 pockmark A and that of GH. This approach can be applied to other similar pockmarks, such as the  
660 Barents Sea pockmarks ([Chand et al., 2009](#)) or in the Norwegian Sea ([Hovland and Svensen,](#)  
661 [2006](#)), in order to define the sub-seabed distribution of GH as well as different formation stages  
662 of the geological features of the study area.

663 For future works, it would be interesting to compare the different shapes of the GHZOZ seen in  
664 [Figure 14](#) to the lithology of the surrounding sediment to highlight how porosity and permeability  
665 contrasts might have contributed to spatial distribution of GH.

666





670

671 *Figure 15. a) Perpendicular cross section across the northern part of pockmark A and b) perpendicular cross section across*  
 672 *the southern part of pockmark. On each cross section GH contents as estimated from in-situ measurements as well as the*  
 673 *GHOZ and fractures/discontinuities as inferred from seismic data are projected.*

674 **6. Conclusion**

675 This paper aims to study the effect of GH content, distribution and morphology on the  
676 geomorphology and the actual state of the pockmarks present in the study area. This work mainly  
677 focused on pockmarks A and C in the Gulf of Guinea, where in-situ acoustic, coring and drilling data  
678 as well as seismic sections were acquired from different oceanographic campaigns. GH contents in  
679 the marine sediment were estimated using the Effective Medium Theory (EMT), which requires an  
680 accurate definition of the mineralogy profile. In cases, where the recovered cores were undisturbed,  
681 the mineral proportions were defined using the XRD and XRF techniques. In cases where the  
682 recovered cores were significantly disturbed due to GH dissociation, a petrophysical model based on  
683 the acoustic data of the site in question was developed and allowed determining the mineral  
684 proportions. The correlations and analysis of this unique database has led to the following  
685 conclusions:

- 686 1. Positive Vp anomalies along with simultaneous increase of the attenuation and applied load  
687 profiles are an indicator of the presence of GH.
- 688 2. A maximum GH content of 26.5% was estimated for a Vp of 2035 m/s using the EMT.
- 689 3. Results derived from the EMT and those from negative thermal and chloride anomalies were  
690 found to yield almost the same GH content.
- 691 4. Correlations between seismic profiles and in-situ data as well as visual observations of  
692 recovered cores have shown that:
  - 693 a. High amplitude chaotic facies are an indicator of the presence of GH. However, low-  
694 amplitude subparallel facies represent undisturbed sediments.
  - 695 b. The study area accommodates zones where solid GH and free gas coexist as well as  
696 zones of free gas pockets.
  - 697 c. Fractures/discontinuities have been identified as preferential pathways in which free  
698 gas can migrate and contribute to further GH formations.

- 699 5. Extrapolation of in-situ and core measurements using seismic data indicate that with a  
700 volume of  $2.7 \times 10^6 m^3$  the GHZOZ occupies 17% of the total volume of pockmark A for an  
701 estimated GH volume of  $0.57 \times 10^6 m^3$ .
- 702 6. The seabed morphology of pockmark A is directly influenced by the distribution of underlying  
703 GH accumulations:
- 704 a. The highest GH contents (20%-30%) are observed to be in the central part of the  
705 pockmark, which is characterised by several bumps.
  - 706 b. The lowest GH contents (0%-10%) are mostly observed at the borders of the  
707 pockmark which are characterised by a slight depression.
- 708 7. The morphology of a given pockmark in the study area might be an indication that can be  
709 used to confirm the presence of GH, determine an interval of GH content and identify  
710 different GH morphologies.

## 711 **Acknowledgments**

712 Data used in the present paper are covered by a confidentiality agreement between Total, Ifremer,  
713 and Marum that restrict access; interested readers can contact the authors for more information. We  
714 The authors would like to thank Natalia Vazquez Riveiros for help in providing the photos of the  
715 forams.

716 The authors would like to express their great appreciation to the *French National Research Agency*  
717 for funding the present study, which is part of the project *HYDRE "Mechanical behaviour of gas-*  
718 *hydrate-bearing sediments"* – ANR-15-CE06-0008.

719 **References**

- 720 Bayon, G., M, H.G., Joel, E., Jean-claude, C., Livio, R., Tania, M., Bernard, D., Eric, C., Michel, V., Nabil,  
721 S., 2015. Achimer U-Th isotope constraints on gas hydrate and pockmark dynamics at the Niger  
722 delta margin 370, 87–98.
- 723 Bastia, R. (2006). An overview of Indian sedimentary basins with special focus on emerging east coast  
724 deepwater frontiers. *The Leading Edge*, 25(7), 818-829.
- 725 Bouriak, S., Vanneste, M., & Saoutkine, A. (2000). Inferred gas hydrates and clay diapirs near the  
726 Storegga Slide on the southern edge of the Vøring Plateau, offshore Norway. *Marine Geology*,  
727 163(1-4), 125-148.
- 728 Brooks, J. M., Bryant, W. R., Bernard, B. B., & Cameron, N. R. (2000). The nature of gas hydrates on  
729 the Nigerian continental slope. *ANNALS-NEW YORK ACADEMY OF SCIENCES*, 912, 76-93.
- 730 Carcione, J. M., & Gei, D. (2004). Gas-hydrate concentration estimated from P-and S-wave velocities  
731 at the Mallik 2L-38 research well, Mackenzie Delta, Canada. *Journal of Applied Geophysics*,  
732 56(1), 73-78.
- 733 Chand, S., & Minshull, T. A. (2003). Seismic constraints on the effects of gas hydrate on sediment  
734 physical properties and fluid flow: a review. *Geofluids*, 3(4), 275-289.
- 735 Chand, S., Minshull, T. A., Gei, D., & Carcione, J. M. (2004). Elastic velocity models for gas-hydrate-  
736 bearing sediments—A comparison. *Geophysical Journal International*, 159(2), 573-590.
- 737 Chand, S., Rise, L., Ottesen, D., Dolan, M.F.J., Bellec, V., Bøe, R., 2009. Pockmark-like depressions near  
738 the Goliat hydrocarbon field , Barents Sea : Morphology and genesis 26, 1035–1042.  
739 <https://doi.org/10.1016/j.marpetgeo.2008.09.002>
- 740 Collett, T., Bahk, J., Boswell, R., Divins, D., Frye, M., Goldberg, D., Husebo, J., Koh, C.A., Malone, M.,  
741 Myres, G., Shipp, C., Torres, M., 2014. Methane Hydrates in Nature- Current Knowledge and  
742 Challenges. *J. Chem. Eng. Data* 60, 319–329.

743 Collett, T., Riedel, M., Cochran, J. R., Boswell, R., Kumar, P., & Sathe, A. V. (2008). Indian continental  
744 margin gas hydrate prospects: results of the Indian National Gas Hydrate Program (NGHP)  
745 expedition 01.

746 Cunningham, R., Lindholm, R.M., 2000. Seismic Evidence for Widespread Gas Hydrate Formation ,  
747 Offshore West Africa 2000.

748 Dai, S., Santamarina, J.C., Waite, W.F., Kneafsey, T.J., 2012. Hydrate morphology: Physical properties  
749 of sands with patchy hydrate saturation. *J. Geophys. Res. B Solid Earth* 117.  
750 <https://doi.org/10.1029/2012JB009667>

751 Damuth, J. E. (1994). Neogene gravity tectonics and depositional processes on the deep Niger Delta  
752 continental margin. *Marine and Petroleum Geology*, 11(3), 320-346.

753 Dewangan, P., Ramprasad, T., Ramana, M. V., Mazumdar, A., Desa, M., & Badesab, F. K. (2010).  
754 Seabed morphology and gas venting features in the continental slope region of Krishna–  
755 Godavari basin, Bay of Bengal: implications in gas-hydrate exploration. *Marine and Petroleum*  
756 *Geology*, 27(7), 1628-1641.

757 Freudenthal, T., Wefer, G., 2015. Drilling cores on the sea floor with the remote-controlled sea floor  
758 drilling rig MeBo. <https://doi.org/10.5194/gi-2-329-2013>

759 Freudenthal, T., Wefer, G., 2007. Scientific Drilling with the Sea Floor Drill Rig MeBo 63–66.  
760 <https://doi.org/10.2204/iodp.sd.5.11.2007>

761 George, R.A.T., Cauquil, E., 2007. AUV Ultrahigh-Resolution 3D Seismic Technique for Detailed  
762 Subsurface Investigations, in: *Offshore Technology Conference*. Houston, Texas, pp. 1–9.

763 Ghosh, R., Sain, K., Ojha, M., 2010. Effective medium modeling of gas hydrate-filled fractures using  
764 the sonic log in the Krishna-Godavari basin, offshore eastern India. *J. Geophys. Res. Solid Earth*  
765 115, 1–15. <https://doi.org/10.1029/2009JB006711>.

766 Guerin, G., Goldberg, D., & Meltser, A. (1999). Characterization of in situ elastic properties of gas

767 hydrate-bearing sediments on the Blake Ridge. *Journal of Geophysical Research: Solid Earth*,  
768 104(B8), 17781-17795.

769 Gullapalli, S., Dewangan, P., Kumar, A., Dakara, G., & Mishra, C. K. (2019). Seismic evidence of free  
770 gas migration through the gas hydrate stability zone (GHSZ) and active methane seep in  
771 Krishna-Godavari offshore basin. *Marine and Petroleum Geology*, 110, 695-705.

772 Helgerud, M.B., Dvorkin, J., Nur, A., Sakai, A., Collett, T., 1999. Elastic wave velocity in marine  
773 sediments with gas hydrates: Effective medium modeling 26, 2021–2024.

774 Helgerud, M.B., Waite, W.F., Kirby, S.H., Nur, A., 2009. Elastic wave speeds and moduli in  
775 polycrystalline ice Ih, si methane hydrate, and sll methane-ethane hydrate. *J. Geophys. Res.*  
776 *Solid Earth* 114, 1–11. <https://doi.org/10.1029/2008JB006132>

777 Holland, M., Schultheiss, P., Roberts, J., Druce, M., 2008. Observed Gas Hydrate Morphologies in  
778 Marine Sediments. *Icgh2008*.

779 Hovland, M., Svensen, H., 2006. Submarine pingoes : Indicators of shallow gas hydrates in a  
780 pockmark at Nyegga , Norwegian Sea 228. *Marine Geology*. 15–23.  
781 <https://doi.org/10.1016/j.margeo.2005.12.005>

782 Jang, J., Santamarina, J.C., 2016. Hydrate bearing clayey sediments: Formation and gas production  
783 concepts. *Mar. Pet. Geol.* 77, 235–246. <https://doi.org/10.1016/j.marpetgeo.2016.06.013>

784 Joshi, A.K., Sain, K., Pandey, L., 2018. Gas hydrate saturation and reservoir characterization at sites  
785 NGHP-02-17 and NGHP-02-19 , Krishna Godavari Basin , eastern margin of India. *Mar. Pet. Geol.*  
786 <https://doi.org/10.1016/j.marpetgeo.2018.06.023>

787 Judd, A., & Hovland, M. (2009). *Seabed fluid flow: the impact on geology, biology and the marine*  
788 *environment*. Cambridge University Press.

789 Ker, S., Gonidec, Y. Le, Gibert, D., 2012. Multiscale seismic attributes: source-corrected wavelet  
790 response and application to high-resolution seismic data. *Geophys. J. Int.* 190, 1746–1760.

791 Kim, H. S., Riedel, M., Ryu, B. J., Kim, G. Y., & Bahk, J. J. (2013). Improving gas hydrate saturation  
792 estimates using P-wave velocity log data by incorporating XRD-Data for detailed matrix-  
793 mineralogy definition. *Marine and Petroleum Geology*, 47, 155-167.

794 Kvenvolden, K.A., 1993. Gas hydrates - Geological perspective and global change. *Rev. Geophys.* 173–  
795 187.

796 Kumar, J., Sain, K., & Arun, K. P. (2019). Seismic attributes for characterizing gas hydrates: a study  
797 from the Mahanadi offshore, India. *Marine Geophysical Research*, 40(1), 73-86.

798 Malinverno, A., Kastner, M., Torres, M.E., Wortmann, U.G., 2008. Gas hydrate occurrence from pore  
799 water chlorinity and downhole logs in a transect across the northern Cascadia margin  
800 (Integrated Ocean Drilling Program Expedition 311). *J. Geophys. Res. Solid Earth* 113, 1–18.  
801 <https://doi.org/10.1029/2008JB005702>

802 Marsset, T., Marsset, B., Ker, S., Thomas, Y., Gall, Y. Le, 2010. Deep-Sea Research I High and very high  
803 resolution deep-towed seismic system : Performance and examples from deep water  
804 *Geohazard studies* 57, 628–637. <https://doi.org/10.1016/j.dsr.2010.01.001>

805 Marsset, T., Ruffine, L., Gay, A., Ker, S., E., C., 2018. Types of fluid-related features controlled by  
806 sedimentary cycles and fault network in deepwater Nigeria 89, 330–349.  
807 <https://doi.org/10.1016/j.marpetgeo.2017.10.004>

808 Riboulot, V., Sultan, N., Imbert, P., Ker, S., 2016. Initiation of gas-hydrate pockmark in deep-water  
809 Nigeria : Geo-mechanical analysis and modelling. *Earth Planet. Sci. Lett.* 434, 252–263.

810 Riedel, M., Collett, T.S., Hyndman, R.D., 2005. GEOLOGICAL SURVEY OF CANADA OPEN FILE 4934 Gas  
811 hydrate concentration estimates from chlorinity , electrical resistivity and seismic velocity  
812 GEOLOGICAL SURVEY OF CANADA OPEN FILE 4934 Gas hydrate concentration estimates from  
813 chlorinity , electrical resistivity and seismic velocity.

814 Riedel, M., Willoughby, E.C., Chen, M.A., He, T., Novosel, I., Schwalenberg, K., Hyndman, R.D.,

815 Spence, G.D., Chapman, N.R., Edwards, R.N., 2006. Gas hydrate on the northern Cascadia  
816 margin : regional geophysics and structural framework 311, 1–28.  
817 <https://doi.org/10.2204/iodp.proc.311.109.2006>

818 Sahling, H., Bohrmann, G., Spiess, V., Bialas, J., Breitzke, M., Ivanov, M., Kasten, S., Krastel, S.,  
819 Schneider, R., 2008. Pockmarks in the Northern Congo Fan area , SW Africa : Complex seafloor  
820 features shaped by fluid flow 249, 206–225. <https://doi.org/10.1016/j.margeo.2007.11.010>

821 Shankar, U., Gupta, D.K., Bhowmick, D., Sain, K., 2013. Gas hydrate and free gas saturations using  
822 rock physics modelling at site NGHP-01-05 and 07 in the Krishna-Godavari Basin, eastern Indian  
823 margin. *J. Pet. Sci. Eng.* 106, 62–70. <https://doi.org/10.1016/j.petrol.2013.04.004>

824 Sloan, E.D., 1998. Gas Hydrates : Review of Physical / Chemical Properties 0624, 191–196.

825 Sultan, N., Bohrmann, G., Ruffine, L., Pape, T., Riboulot, V., Colliat, J.L., Prunele, A.D., Dennielou, B.,  
826 Garziglia, S., Himmler, T., Marsset, T., Peters, C. a., Rabiou, a., Wei, J., 2014. *Journal of*  
827 *Geophysical Research : Solid Earth.* *J. Geophys. Res. Earth* 119, 2679–2694.  
828 <https://doi.org/10.1029/2010JB007453>.Pockmark

829 Sultan, N., Garziglia, S., Ruffine, L., 2016. New insights into the transport processes controlling the  
830 sulfate-methane-transition-zone near methane vents. *Sci. Rep.* 6, 1–9.  
831 <https://doi.org/10.1038/srep26701>

832 Sultan, N., Marsset, B., Ker, S., Marsset, T., Voisset, M., Vernant, A.M., Bayon, G., Cauquil, E., Adamy,  
833 J., Colliat, J.L., Drapeau, D., 2010. Hydrate dissolution as a potential mechanism for pockmark  
834 formation in the Niger delta. *J. Geophys. Res. Solid Earth* 115, 1–33.  
835 <https://doi.org/10.1029/2010JB007453>

836 Sultan, N., Voisset, M., Marsset, T., Vernant, A. M., Cauquil, E., Colliat, J. L., & Curinier, V., 2007.  
837 Detection of free gas and gas hydrate based on 3D seismic data and cone penetration testing:  
838 An example from the Nigerian Continental Slope. *Marine Geology*, 240(1-4), 235-255.

839 Taleb, F., Garziglia, S., Sultan, N., 2018. *Journal of Geophysical Research : Solid Earth*

840 Hydromechanical Properties of Gas Hydrate-Bearing Fine Sediments From In Situ Testing  
841 Journal of Geophysical Research : Solid Earth 9615–9634.  
842 <https://doi.org/10.1029/2018JB015824>

843 Torres, M.E., Wallmann, K., Tre, A.M., Bohrmann, G., Borowski, W.S., Tomaru, H., 2004. Gas hydrate  
844 growth , methane transport , and chloride enrichment at the southern summit of Hydrate Ridge  
845 , Cascadia margin off Oregon 226, 225–241. <https://doi.org/10.1016/j.epsl.2004.07.029>

846 Ussler III, W., & Paull, C. K., 2001. Ion exclusion associated with marine gas hydrate deposits.  
847 Washington DC American Geophysical Union Geophysical Monograph Series, 124, 41-51.

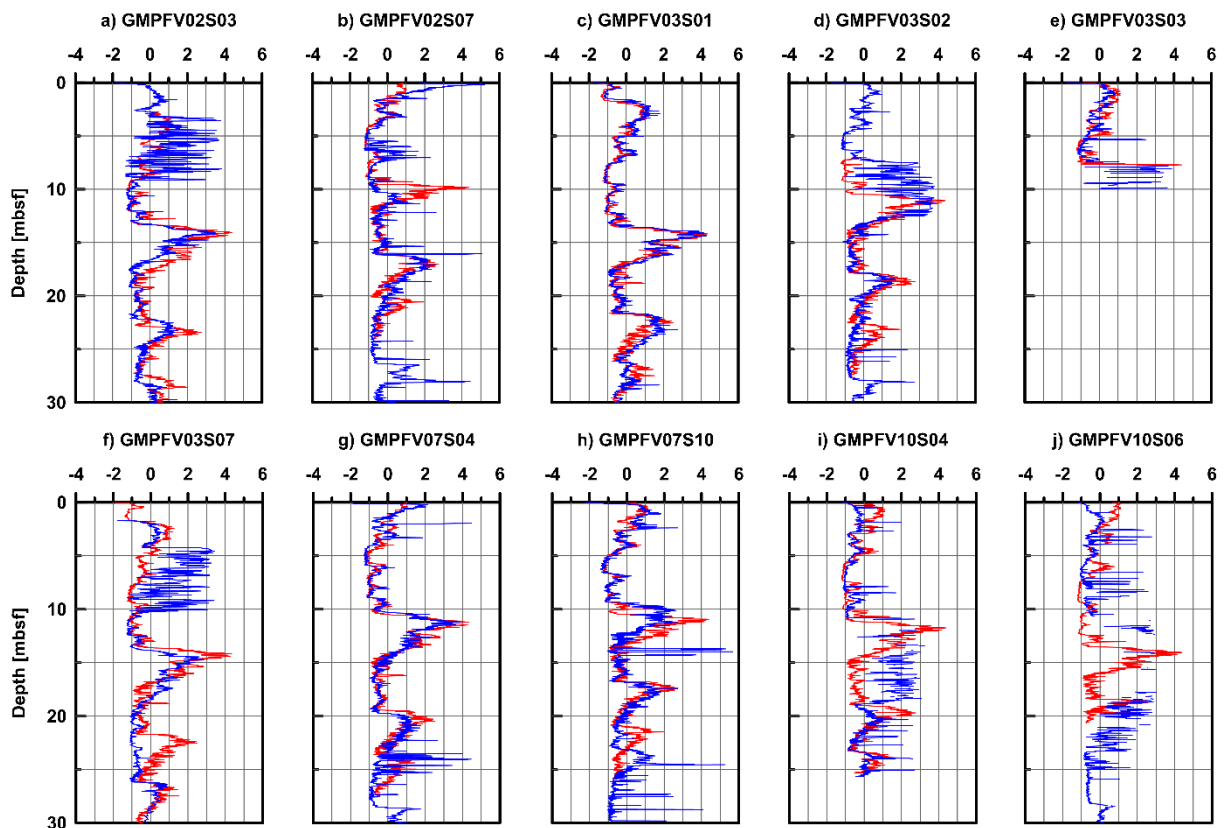
848 Vaular, E.N., Barth, T., Haflidason, H., 2010. Organic Geochemistry The geochemical characteristics of  
849 the hydrate-bound gases from the Nyegga pockmark field , Norwegian Sea. Org. Geochem. 41,  
850 437–444. <https://doi.org/10.1016/j.orggeochem.2010.02.005>

851 Waite, W.F., Santamarina, J.C., Cortes, D.D., Dugan, B., Espinoza, D.N., Germaine, J., Jang, J., Jung,  
852 J.W., Kneafsey, T.J., Shin, H., Soga, K., Winters, W.J., 2009. PHYSICAL PROPERTIES OF HYDRATE-  
853 BEARING SEDIMENTS 1–38. <https://doi.org/10.1029/2008RG000279>.

854 Wang, X., Hutchinson, D. R., Wu, S., Yang, S., & Guo, Y. (2011). Elevated gas hydrate saturation within  
855 silt and silty clay sediments in the Shenhu area, South China Sea. Journal of Geophysical  
856 Research: Solid Earth, 116(B5).

857 Wei, J., Pape, T., Sultan, N., Colliat, J.L., Himmler, T., Ruffine, L., de Prunelé, A., Dennielou, B.,  
858 Garziglia, S., Marsset, T., Peters, C.A., Rabiou, A., Bohrmann, G., 2015. Gas hydrate distributions  
859 in sediments of pockmarks from the Nigerian margin - Results and interpretation from shallow  
860 drilling. Mar. Pet. Geol. 59, 359–370. <https://doi.org/10.1016/j.marpetgeo.2014.09.013>

861 Wood, W. T., Gettrust, J. F., Chapman, N. R., Spence, G. D., & Hyndman, R. D. (2002). Decreased  
862 stability of methane hydrates in marine sediments owing to phase-boundary roughness.  
863 Nature, 420(6916), 656.



865  
 866 *Figure A. Correlations between attenuations of compressional waves at reference site (red profiles) and GH bearing sites*  
 867 *(blue profiles): a) GMPFV02S03, b) GMPFV02S07, c) GMPFV03S01, d)GMPFV03S02, e) GMPFV03S03, f) GMPFV03S07, g)*  
 868 *GMPFV07S04, h) GMPFV07S10,i) GMPFV10S04, j) GMPFV10S06*

869 **Figure A** shows correlations between attenuation profiles of compressional waves from GH bearing  
 870 sediments (blue profiles) and those from reference sites (red profiles). Depth corrections between  
 871 both profiles have allowed determining new depth-adjusted attenuation profiles at GH bearing sites;  
 872 and, eventually use these profiles to define the mineral proportions needed in order to estimat GH  
 873 content (see section 4: Mineralogy analysis).

875 **Appendix B – Assumptions made in order to apply the effective medium theory**

876 Assumptions and correlations were carried out throughout this work in order to apply the EMT.

877 The following critical parametric study aims to quantify the error resulting from this process; thus,

878 two uncertainties are discussed: a) the assumed constant value of the quartz profile and b) the

879 assumed values of  $C_c$  and  $e_0$  values. The residual error is calculated using the following equation:

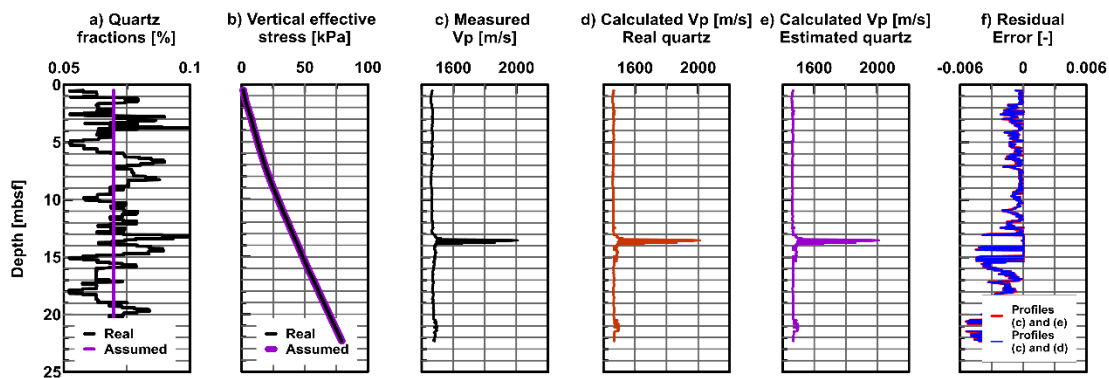
880 
$$\text{Residual error} = \ln \frac{x_{\text{assumed}}}{x_{\text{actual}}} \quad (8)$$

881 **a) Mineralogy profile (assumed constant value of quartz)**

882 After defining the calcite fractions, the quartz quantity was assumed constant with depth and

883 equal to the average value of the quartz fraction at reference site. This allowed defining the

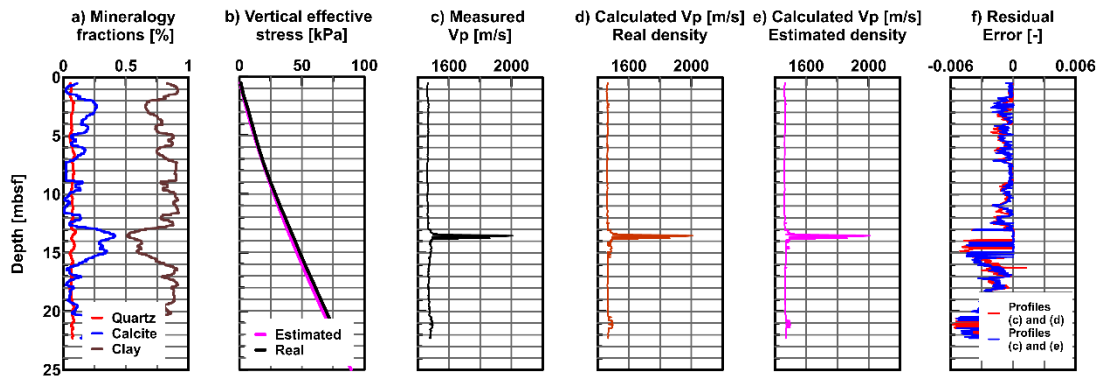
884 clay fraction using equation 3.



886 *Figure B1. Parametric study accounting for the constant quartz assumption: a) measured and averaged quartz profiles from*  
887 *core GMCS05, b) vertical effective stress profile using the measured and averaged quartz value, c) Measured P-wave velocity*  
888 *at reference site GMPFV07S01, d) Calculated P-wave velocity using measured quartz value, e) Calculated P-wave velocity*  
889 *using averaged quartz value, f) residual error between measured and calculated P-wave velocity using measured quartz*  
890 *value and between measured and calculated P-wave velocity using averaged quartz value.*

891  
892  
893  
894  
895  
896

897 **b) Density profile (assumed  $C_c$  and  $e_0$  values)**



899 *Figure B2. Parametric study accounting for assumed  $C_c$  and  $e_0$  values: a) Mineralogy fractions from core GMCS05, b) vertical*  
900 *effective stress profile using real and assumed  $C_c$  and  $e_0$  values, c) Measured P-wave velocity at reference site GMPFV07S01,*  
901 *d) Calculated P-wave velocity using real  $C_c$  and  $e_0$  values, e) Calculated P-wave velocity using estimated  $C_c$  and  $e_0$  values, f)*  
902 *residual error between measured and calculated P-wave velocity using real  $C_c$  and  $e_0$  values and between measured and*  
903 *calculated P-wave velocity using assumed  $C_c$  and  $e_0$  values.*